

# Weierstraß-Institut für Angewandte Analysis und Stochastik

im Forschungsverbund Berlin e.V.

Preprint

ISSN 0946 – 8633

## Comparison of numerical methods for the reconstruction of elastic obstacles from the far-field data of scattered acoustic waves

Johannes Elschner<sup>1</sup>, George C. Hsiao<sup>2</sup>, Andreas Rathsfeld<sup>1</sup>

submitted: 22 January 2010

<sup>1</sup> Weierstrass Institute  
for Applied Analysis and Stochastics  
Mohrenstr. 39  
10117 Berlin  
Germany  
E-Mail: [elschner@wias-berlin.de](mailto:elschner@wias-berlin.de)  
[rathsfeld@wias-berlin.de](mailto:rathsfeld@wias-berlin.de)

<sup>2</sup> University of Delaware  
Department of Mathematical Sciences  
Newark, Delaware 19716–2553  
USA  
E-Mail: [hsiao@math.udel.edu](mailto:hsiao@math.udel.edu)

No. 1479  
Berlin 2010



---

2000 *Mathematics Subject Classification.* 35R30 76Q05 35J05.

*Key words and phrases.* acoustic and elastic waves, inverse scattering, simple Newton iteration, Kirsch-Kress method.

Edited by  
Weierstraß-Institut für Angewandte Analysis und Stochastik (WIAS)  
Mohrenstraße 39  
10117 Berlin  
Germany

Fax: + 49 30 2044975  
E-Mail: [preprint@wias-berlin.de](mailto:preprint@wias-berlin.de)  
World Wide Web: <http://www.wias-berlin.de/>

## Abstract

We consider the inverse problem for an elastic body emerged in a fluid due to an acoustic wave. The shape of this obstacle is to be reconstructed from the far-field pattern of the scattered wave. For the numerical solution in the two-dimensional case, we compare a simple Newton type iteration method with the Kirsch-Kress algorithm. Our computational tests reveal that the Kirsch-Kress method converges faster for obstacles with very smooth boundaries. The simple Newton method, however, is more stable in the case of not so smooth domains and more robust with respect to measurement errors.

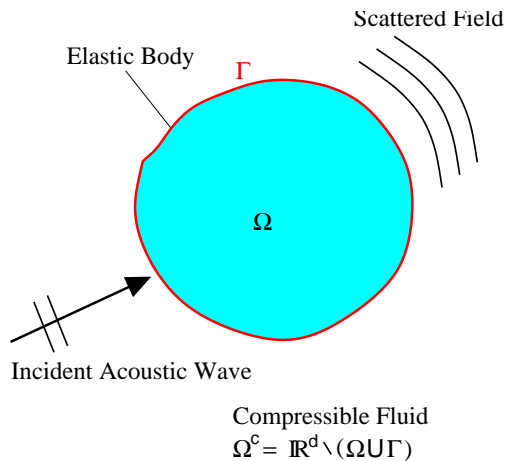


Figure 1: Acoustic wave and obstacle.

## 1 Introduction

If an elastic body is subject to an acoustic wave propagating through the surrounding fluid, then an elastic wave is generated inside the body, and the acoustic wave is perturbed (cf. Figure 1). The wave perturbation is characterized by the asymptotics of the scattered field, namely, the far-field pattern. Suppose the material properties of body and surrounding fluid are known. Then the usual inverse problem of obstacle scattering is to determine the shape of the body from measured far-field data generated by plane waves incident from one or from a finite number of directions. This problem is extremely ill-posed such that regularization techniques are needed for the solution.

Clearly, the same numerical methods used for the inverse problems for obstacles with sound-hard and sound-soft boundaries or for penetrable obstacles can be adapted to the scattering by elastic bodies. Among the available numerical methods, in recent years factorization methods are very popular (cf. e.g. [11]). Without any a priori information about geometrical details like connectivity components or holes, these methods provide good approximations for the shape of the obstacle. The case of acoustic scattering by

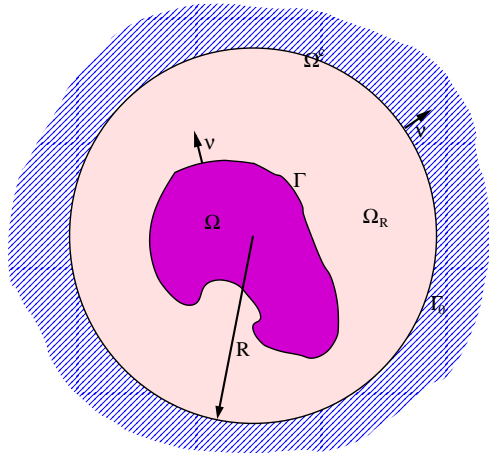


Figure 2: Domains.

elastic bodies in [15] is treated by the linear sampling method. Classical methods such as in [3, 14] (cf. [4] for the case of scattering by elastic obstacles) generally require more information on the geometry of the obstacle. For instance, the boundary of the obstacle is required to be homeomorphic to a circle for 2-D and to a sphere for 3-D problems, respectively. Starting from a reasonable initial guess, the parametrization of the obstacle boundary is approximated in a Newton type iteration. Though the accuracy of the reconstructed solution is always limited by the ill-posedness, we expect the classical Newton approach to be more accurate than the factorization methods. To avoid the solution of direct problems in each step of iteration, besides the boundaries also the wave field can be included into the components of the iterative solutions. For instance, a method proposed by Kirsch and Kress (cf. e.g. [12, 3, 20] and cf. [5] for the case of scattering by elastic obstacles) represents the waves by potentials with generating layer functions defined over artificial curves. Note that, for inverse problems in acoustic scattering by elastic obstacles, difficulties with unpleasant eigensolutions of the direct problem, referred to as Jones modes, can be avoided if the Kirsch-Kress method is applied.

In this paper we consider the two-dimensional case and compare the simple Newton method of [4] with the Kirsch-Kress method of [5] for which we present numerical results for the first time. We start discussing the solution of the direct problem in Section 2. Using the direct solution, we introduce the two numerical schemes for the inverse problem in Section 3. Then we recall the convergence results from [4, 5]. In Section 4 we discuss some details of the implementation. Finally, we present numerical results in Section 5. Our results show that the Kirsch-Kress method converges faster for obstacles with very smooth boundaries. The simple Newton method, however, is more stable in the case of not so smooth domains and more robust with respect to measurement errors.

## 2 Direct problem: Elastic obstacle in fluid

Suppose a bounded elastic body is emerged in a homogeneous compressible inviscid fluid. We denote the domain of the body by  $\Omega$ , its boundary curve by  $\Gamma$  (cf. Figure 2), and

assume that an incoming plane wave is moving in the exterior  $\Omega^c := \mathbb{R}^2 \setminus \Omega$  toward the body. This wave is scattered by the body and generates an elastic wave inside the body. Mathematically, the acoustic wave is described by the pressure perturbation  $p$  over  $\Omega^c$  and by the displacement function  $u$  on  $\Omega$ . The displacement fulfills the Navier (time-harmonic Lamé) equation

$$\begin{aligned} \Delta^* u(x) + \varrho \omega^2 u(x) &= 0, \quad x \in \Omega, \\ \Delta^* u(x) &:= \mu \Delta u(x) + (\lambda + \mu) \nabla [\nabla \cdot u(x)]. \end{aligned} \quad (2.1)$$

Here  $\omega$  is the frequency,  $\varrho$  the density of body, and  $\lambda, \mu$  are the Lamé constants. The total pressure  $p$  is the sum of the incoming wave  $p^{inc}$  and the scattered wave  $p^s$  which satisfies the Helmholtz equation and the radiation condition at infinity

$$\Delta p^s(x) + k_w^2 p^s(x) = 0, \quad x \in \Omega^c, \quad (2.2)$$

$$\frac{x}{|x|} \cdot \nabla p^s(x) - ik_w p^s(x) = o(|x|^{-1/2}), \quad |x| \rightarrow \infty, \quad (2.3)$$

where  $k_w^2 = \omega^2/c^2$  is the wave number and  $c$  the speed of sound. The pressure and the displacement field are coupled through the transmission conditions

$$u(x) \cdot \nu(x) = \frac{1}{\varrho_f \omega^2} \left\{ \frac{\partial p^s(x)}{\partial \nu} + \frac{\partial p^{inc}(x)}{\partial \nu} \right\}, \quad x \in \Gamma, \quad (2.4)$$

$$t[u](x) = -\{p^s(x) + p^{inc}(x)\} \nu(x), \quad x \in \Gamma, \quad (2.5)$$

$$t[u](x) := 2\mu \frac{\partial u}{\partial \nu} \Big|_{\Gamma} + \lambda [\nabla \cdot u] \nu \Big|_{\Gamma} + \mu \nu \times [\nabla \times u] \Big|_{\Gamma}$$

$$\nu \times [\nabla \times u] \Big|_{\Gamma} := \begin{pmatrix} \nu_2 (\partial_{x_1} u_2 - \partial_{x_2} u_1) \\ \nu_1 (\partial_{x_2} u_1 - \partial_{x_1} u_2) \end{pmatrix} \Big|_{\Gamma}.$$

Here  $\varrho_f$  is the density of the fluid and  $\nu$  denotes the unit normal at the points of  $\Gamma$  exterior with respect to  $\Omega$ .

For numerical computations, we truncate the exterior domain  $\Omega^c$  to the annular domain  $\Omega_R$  with the outer boundary  $\Gamma_0$ . The Helmholtz equation (2.2) is solved over  $\Omega_R$

$$\Delta p^s(x) + k_w^2 p^s(x) = 0, \quad x \in \Omega_R \quad (2.6)$$

and the nonlocal boundary condition

$$V_{\Gamma_0}^{ac} [\partial_{\nu} p^s|_{\Gamma_0}](x) + \frac{1}{2} [p^s|_{\Gamma_0}](x) - K_{\Gamma_0}^{ac} [p^s|_{\Gamma_0}](x) = 0, \quad x \in \Gamma_0, \quad (2.7)$$

$$K_{\Gamma_0}^{ac} p(x) := \int_{\Gamma_0} \frac{\partial G(x, y; k_w)}{\partial \nu(y)} p(y) d_{\Gamma_0} y,$$

$$V_{\Gamma_0}^{ac} \sigma(x) := \int_{\Gamma_0} G(x, y; k_w) \sigma(y) d_{\Gamma_0} y,$$

$$G(x, y; k_w) := \frac{\mathbf{i}}{4} H_0^{(1)}(k_w |x - y|) \quad (2.8)$$

is imposed, where  $H_0^{(1)}$  is the Hankel function of the first kind and of order 0 (cf. the boundary integral equation techniques in [10]). The corresponding variational formulation

of (2.1), (2.6), (2.4), (2.5), and (2.7) takes the form: Find  $(u, p^s, \sigma)$  with  $u \in [H^1(\Omega)]^2$ ,  $p^s \in H^1(\Omega_R)$ , and  $\sigma \in H^{-1/2}(\Gamma_0)$  such that

$$\mathcal{B}\left((u, p^s, \sigma)^\top, (v, q^s, \chi)^\top\right) = \mathcal{R}\left(p^{inc}, (v, q^s, \chi)^\top\right) := \begin{pmatrix} -\int_\Gamma p^{inc} \nu \cdot \bar{v} \\ \int_\Gamma \frac{\partial p^{inc}}{\partial \nu} \bar{q}^s \\ 0 \end{pmatrix} \quad (2.9)$$

is valid for any  $v \in [H^1(\Omega)]^2$ ,  $q^s \in H^1(\Omega_R)$ , and  $\chi \in H^{-1/2}(\Gamma_0)$ . The sesqui-linear form  $\mathcal{B}$  is given by

$$\begin{aligned} \mathcal{B}\left((u, p^s, \sigma)^\top, (v, q^s, \chi)^\top\right) &:= \begin{pmatrix} a\left((u, p^s, \sigma)^\top, (v, q^s, \chi)^\top\right) \\ b\left((u, p^s, \sigma)^\top, (v, q^s, \chi)^\top\right) \\ c\left((u, p^s, \sigma)^\top, (v, q^s, \chi)^\top\right) \end{pmatrix}, \\ a\left((u, p^s, \sigma)^\top, (v, q^s, \chi)^\top\right) &:= \int_\Omega \left\{ \lambda \nabla \cdot u \overline{\nabla \cdot v} + \frac{\mu}{2} \sum_{i,j=1}^d [\partial_i u_j \overline{\partial_j v_i} + \partial_i u_j \overline{\partial_i v_j}] \right. \\ &\quad \left. - \rho \omega^2 u \cdot \bar{v} \right\} + \int_\Gamma p^s n \cdot \bar{v}, \\ b\left((u, p^s, \sigma)^\top, (v, q^s, \chi)^\top\right) &:= \int_{\Omega_R} \left\{ \nabla p^s \cdot \overline{\nabla q^s} - k_w^2 p^s \bar{q}^s \right\} + \rho_f \omega^2 \int_\Gamma u^- \cdot n \bar{q}^s \\ &\quad - \int_{\Gamma_0} \sigma \bar{q}, \\ c\left((u, p^s, \sigma)^\top, (v, q^s, \chi)^\top\right) &:= \int_{\Gamma_0} \left\{ V_{\Gamma_0}^{ac} \sigma + \left( \frac{1}{2} I - K_{\Gamma_0}^{ac} \right) p^s \right\} \bar{\chi}. \end{aligned}$$

The system (2.9) can be solved by the finite element method. Suppose the boundary  $\Gamma$  of the obstacle is piecewise smooth and choose the auxiliary curves  $\Gamma_0$  such that the corresponding interior domain has no Dirichlet eigenvalue equal to  $k_w^2$  for the negative Laplacian. Then existence and uniqueness of the variational solutions as well as the convergence of the finite element method (cf. [4]) can be shown whenever there is no nontrivial solution  $u_0$  of

$$\begin{aligned} \Delta^* u_0(x) + \rho \omega^2 u_0(x) &= 0, \quad x \in \Omega, \\ t[u_0](x) &= 0, \quad x \in \Gamma, \\ u_0(x) \cdot \nu &= 0, \quad x \in \Gamma. \end{aligned} \quad (2.10)$$

Note that nontrivial solutions of (2.10) are called Jones modes, and a frequency  $\omega$ , for which the given domain  $\Omega$  has a nontrivial solution of (2.10), is called Jones frequency. It is known that domains with Jones frequencies exist at least in the three-dimensional case, but are exceptional (cf. [16, 8]).

Alternatively to the finite element solution, the complete pressure function and the displacement field can be approximated by potentials with sources over auxiliary curves (cf. Figure 3). We introduce the curve  $\Gamma_i$  “close” to  $\Gamma$ , but inside  $\Omega$ , and the curve  $\Gamma_e$  in  $\Omega_R$  surrounding  $\Gamma$ . We represent the pressure and the displacement by

$$p^s(x) = [V_{\Gamma_i}^{ac} \varphi_i](x), \quad x \in \Omega^c, \quad u(x) = [V_{\Gamma_e}^{el} \vec{\varphi}_e](x), \quad x \in \Omega \quad (2.11)$$

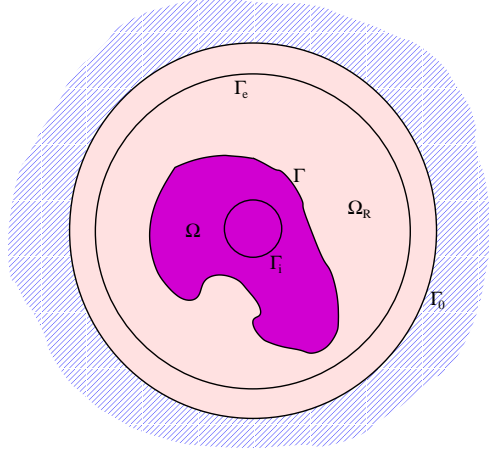


Figure 3: Domains and auxiliary curves

with a scalar layer function  $\varphi_i$  and a vector layer  $\vec{\varphi}_e$ . The potentials are defined by

$$[V_\Lambda^{ac}p](x) := \int_\Lambda p(y)G(x, y; k_\omega) d_\Lambda y, \quad x \in \mathbb{R}^2, \quad (2.12)$$

$$[V_\Lambda^{el}u](x) := \int_\Lambda G^{el}(y, x)u(y) d_\Lambda y, \quad x \in \mathbb{R}^2, \quad (2.13)$$

$$G^{el}(y, x) := \frac{1}{\mu} \left( G(x, y; k_s)\delta_{ij} + \frac{1}{k_s^2} \frac{\partial^2}{\partial x_i \partial x_j} (G(x, y; k_s) - G(x, y; k_p)) \right)_{i,j=0}^2,$$

where the fundamental solution  $G(\cdot, \cdot; k)$  is given in (2.8) and the wave numbers  $k_p$  and  $k_s$  are defined by  $\varrho\omega^2 = (\lambda + 2\mu)k_p^2 = \mu k_s^2$ . The layer functions in (2.12) and (2.13) are chosen such that the corresponding pressure and displacements fields satisfy the transmission conditions (2.4) and (2.5). In other words, to get a good approximate solution we have to solve the integral equations

$$t[V_{\Gamma_e}^{el}\vec{\varphi}_e](x) + [V_{\Gamma_i}^{ac}\varphi_i](x)\nu(x) = -p^{inc}\nu(x), \quad x \in \Gamma, \quad (2.14)$$

$$\varrho_f\omega^2\nu(x) \cdot [V_{\Gamma_e}^{el}\vec{\varphi}_e](x) - \partial_\nu[V_{\Gamma_i}^{ac}\varphi_i](x) = \partial_\nu p^{inc}(x), \quad x \in \Gamma. \quad (2.15)$$

Numerical methods based on the discretization of (2.12), (2.13), (2.14) and (2.15) are well-known to exhibit high rates of convergence (cf. e.g. Sect. 9.8 in [6] and [2, 7, 9]). However, for not so simple geometries, an appropriate choice of  $\Gamma_i$  and  $\Gamma_e$  and an appropriate quadrature of the integrals is not trivial. A bad choice may lead to extremely ill-posed equations (2.14), (2.15) and to false results.

For a point  $x$  tending to infinity, the scattered pressure field  $p^s(x)$  is known to have the following asymptotics

$$p^s(x) = \frac{e^{ik_\omega|x|}}{|x|^{1/2}} p^\infty\left(\frac{x}{|x|}\right) + \mathcal{O}\left(\frac{1}{|x|^{3/2}}\right), \quad |x| \rightarrow \infty, \quad (2.16)$$

$$p^\infty(e^{it}) = \frac{e^{i\pi/4}}{\sqrt{8\pi k_\omega}} \int_{\Gamma_i} \left\{ [ik_\omega \nu_y \cdot e^{it}] p(y) + \partial_\nu p(y) \right\} e^{-ik_\omega y \cdot e^{it}} d_{\Gamma_i} y.$$

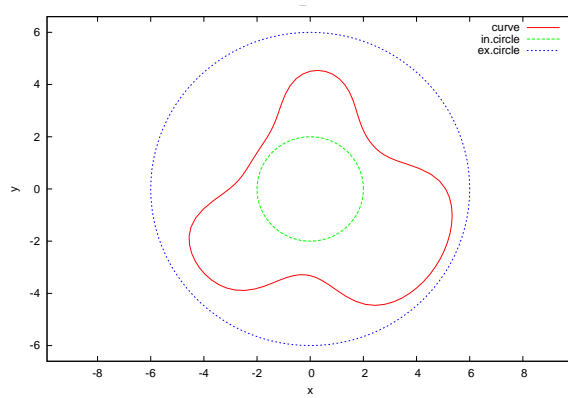


Figure 4: Geometry of scatterer.

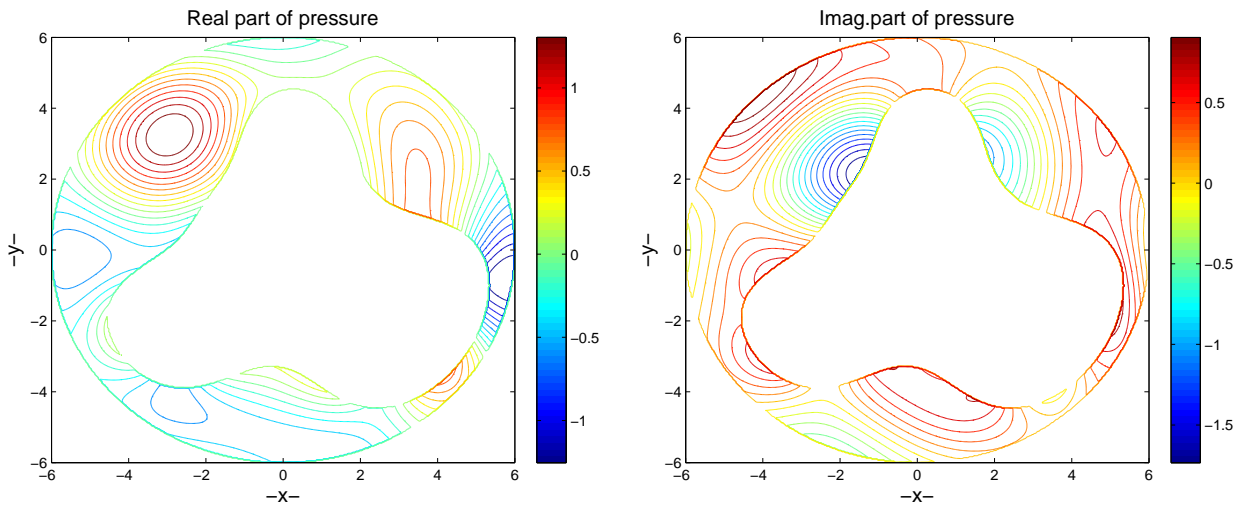


Figure 5: Pressure field: real and imaginary parts.

The function  $\mathcal{F}[p^s](t) := p^\infty(e^{it})$  is called the far-field pattern of the scattered field. This is the entity which can be measured.

We conclude this section by a numerical example. If we choose the nonconvex domain with boundary curve  $\Gamma$  according to Figure 4, the constants

$$\begin{aligned}
 \omega &= 1.5707963267948966 \text{ kHz}, & \varrho &= 6.75 \cdot 10^{-8} \text{ kg/m}^3, \\
 \lambda &= 1.287373095 \text{ Pa}, & \mu &= 0.66315 \text{ Pa}, \\
 c &= 1500 \text{ m/s}, & \varrho_f &= 2.5 \cdot 10^{-8} \text{ kg/m}^3,
 \end{aligned} \tag{2.17}$$

and the direction of the incoming plane wave equal to  $v = (1, 0)^\top$ , then we get by the finite element method [4] the pressure function, the displacement field, and the far-field pattern plotted in Figures 5-8.



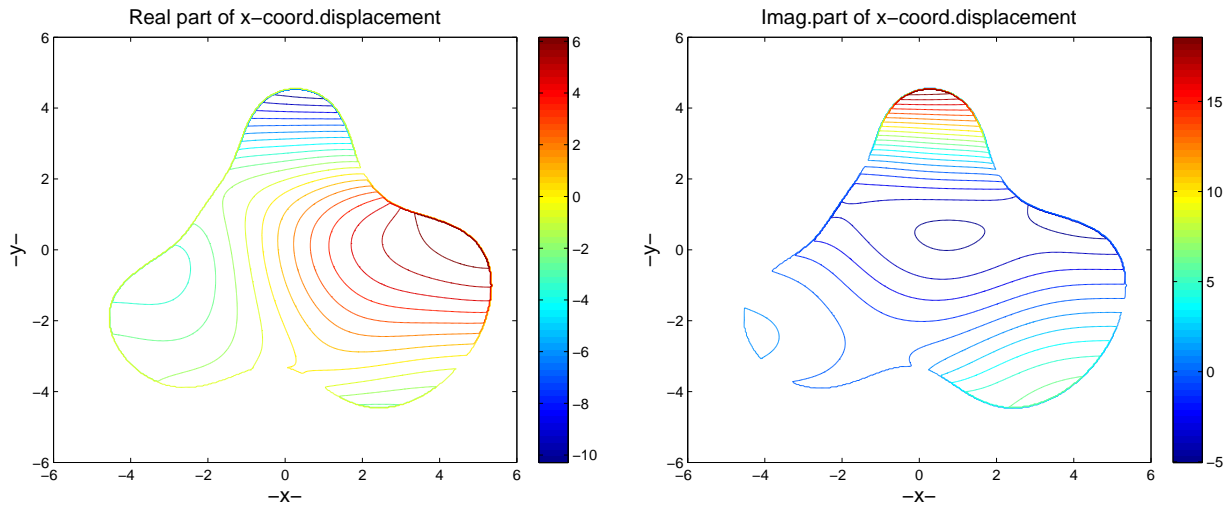


Figure 6: x-component of displacement field: real and imaginary parts.

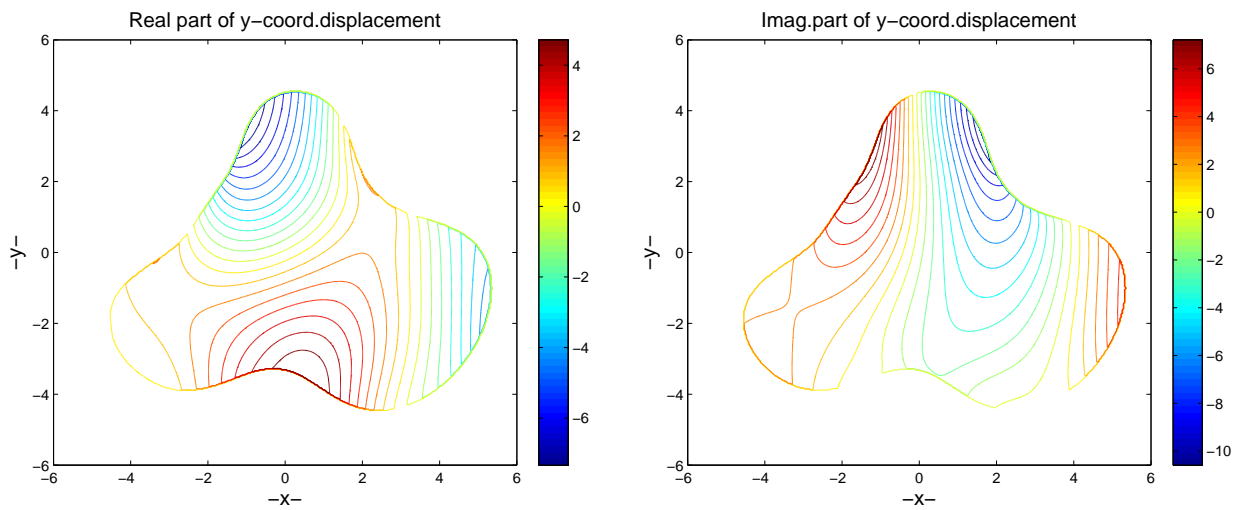


Figure 7: y-component of displacement field: real and imaginary parts.

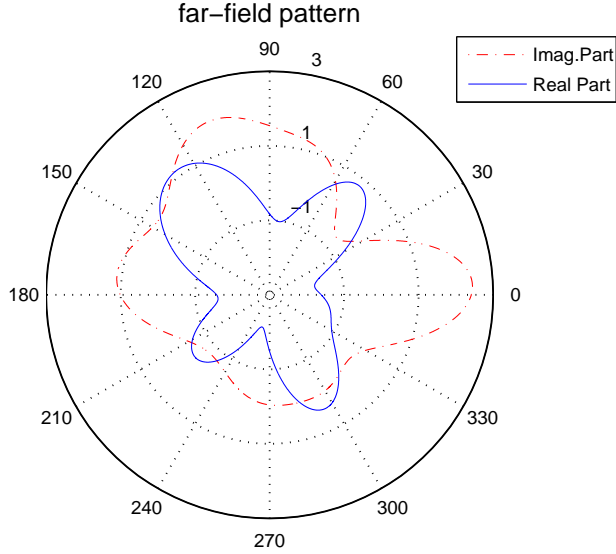


Figure 8: Far-field pattern.

### 3 Inverse problem and iterative approximation

Now we suppose that the boundary curve  $\Gamma$  of the obstacle is star-shaped and included between the inner curve  $\Gamma_i := \{x \in \mathbb{R}^2 : |x| = r_i\}$  and the outer curve  $\Gamma_e := \{x \in \mathbb{R}^2 : |x| = r_e\}$ , i.e.,

$$\Gamma := \{\mathbf{r}(t)e^{it} : 0 \leq t \leq 2\pi\}, \quad \mathbf{r}(t) = \hat{a}_0 + \sum_{j=1}^{\infty} \{\hat{a}_j \cos(jt) + \hat{b}_j \sin(jt)\}$$

with the constraint  $r_i < \mathbf{r}(t) < r_e$ ,  $0 \leq t \leq 2\pi$ . To avoid this constraint, we can use the parametrization

$$\Gamma = \Gamma^{\mathbf{r}} := \{\tilde{\mathbf{r}}(t)e^{it} : 0 \leq t \leq 2\pi\}, \quad \tilde{\mathbf{r}}(t) := \frac{r_e + r_i}{2} + \frac{r_e - r_i}{\pi} \arctan(\mathbf{r}(t)). \quad (3.1)$$

Having in mind this representation, the star-shaped curve is uniquely determined by the real valued function  $\mathbf{r}$  or, equivalently, by the Fourier coefficients  $\{\hat{a}_j, \hat{b}_j\}$ . The direct problem of the previous section defines a continuous mapping (cf. [4])

$$F : H_{per}^{1+\varepsilon}[0, 2\pi] \longrightarrow L_{per}^2[0, 2\pi], \quad \Gamma^{\mathbf{r}} \mapsto p^\infty,$$

where  $p^\infty = \mathcal{F}[p^s]$  is the far-field of the scattered field  $p^s$ , and  $p^s$  is the pressure part of the solution  $(p^s, u)$  to the direct problem (2.1), (2.6), (2.4), (2.5), and (2.7) including the interface  $\Gamma = \Gamma^{\mathbf{r}}$  and a fixed incoming plane wave  $p^{inc}$ . The space  $H_{per}^{1+\varepsilon}[0, 2\pi]$  is the periodic Sobolev space of order  $1 + \varepsilon > 1$  over the interval  $[0, 2\pi]$ .  $L^2[0, 2\pi]$  is the corresponding Lebesgue space. Now the inverse problem is the following: For a given far-field pattern  $p^\infty$ , find the shape of the obstacle with boundary  $\mathbf{r}_{sol}$  such that the scattered field corresponding to the fixed incoming plane wave  $p^{inc}$  has the far-field pattern  $p^\infty$ , i.e., such that  $F(\mathbf{r}_{sol}) = p^\infty$ . To our knowledge, results on the uniqueness of the solution  $\mathbf{r}_{sol}$  are not known yet.

We now define three different optimization problems equivalent to the inverse problem. Numerical algorithms for the inverse problem can be derived simply by applying numerical minimization schemes to the optimization problems. More precisely, the minimization schemes are applied to regularized modifications of the optimization problems.

The first optimization problem is to find a least-squares solution  $\mathbf{r}_{min}$ , i.e., a minimizer of the following problem

$$\inf_{\mathbf{r} \in H_{per}^{1+\varepsilon}[0, 2\pi]} \mathcal{J}_\gamma(\mathbf{r}), \quad \mathcal{J}_\gamma(\mathbf{r}) := \|F(\mathbf{r}) - p^\infty\|_{L^2[0, 2\pi]}^2.$$

Since the inverse problem is ill-posed and since the measured far-field data is given with noise, we replace the last optimization problem by

$$\inf_{\mathbf{r} \in H_{per}^{1+\varepsilon}[0, 2\pi]} \mathcal{J}_\gamma^1(\mathbf{r}), \quad \mathcal{J}_\gamma^1(\mathbf{r}) := \|F(\mathbf{r}) - p_{noisy}^\infty\|_{L^2[0, 2\pi]}^2 + \gamma \|\mathbf{r}\|_{H_{per}^{1+\varepsilon}[0, 2\pi]}^2, \quad (3.2)$$

where  $\gamma$  is a small positive regularization parameter. As usual this parameter is to be chosen in dependence on the noise level. To guarantee convergence for noise level tending to zero and for  $\gamma \rightarrow 0$ , we suppose

$$\|p^\infty - p_{noisy}^\infty\|_{L^2[0, 2\pi]}^2 \leq c\gamma \quad (3.3)$$

for a constant  $c$  independent of  $\gamma$ . The first numerical algorithm (cf. [4]) consists now in discretizing the mapping  $F$  by finite elements and applying a Gauss-Newton method to determine a minimizer of (3.2). This is a modified Newton method for the operator equation  $F(\mathbf{r}_{sol}) = p_{noisy}^\infty$  which we shall call the simple Newton iteration.

**Theorem 3.1 ([4])** *Suppose  $\Gamma_0$  is chosen such that the corresponding interior domain has no Dirichlet eigenvalue equal to  $k_\omega^2$  for the negative Laplacian. Then we have:*

- i) For any  $\gamma > 0$ , there is a unique minimizer  $\mathbf{r}^\gamma$  of (3.2).*
- ii) Suppose  $\mathbf{r}^\gamma$  is a set of minimizers for (3.2). Then the minima of the functionals,  $\mathcal{J}_\gamma^1(\mathbf{r}^\gamma)$ , tend to  $\inf_{\mathbf{r} \in H_{per}^{1+\varepsilon}[0, 2\pi]} \mathcal{J}_0^1(\mathbf{r})$  for  $\gamma \rightarrow 0$ .*
- iii) Suppose the far-field pattern  $p^\infty$  is the exact pattern for a fixed solution  $\mathbf{r}^*$  of the inverse problem, i.e.,  $F(\mathbf{r}^*) = p^\infty$  and  $\mathcal{J}_0^1(\mathbf{r}^*) = 0$ . Then, for  $\varepsilon > 0$  and for any set of minimizers  $\mathbf{r}^\gamma$ , there exists a subsequence  $\mathbf{r}^{\gamma_n}$  converging weakly in  $H_{per}^{1+\varepsilon}[0, 2\pi]$  and strongly in  $H_{per}^{1+\varepsilon'}[0, 2\pi]$ ,  $0 < \varepsilon' < \varepsilon$ , to a solution  $\mathbf{r}^{**}$  of (3.2) with  $\gamma = 0$  and, therewith, to a solution of the inverse problem.*
- iv) If, additionally to the assumptions of iii), the solution  $\mathbf{r}^*$  of the inverse problem is unique, then we even get that  $\mathbf{r}^\gamma$  tends to  $\mathbf{r}^*$  weakly in  $H_{per}^{1+\varepsilon}[0, 2\pi]$  and strongly in  $H_{per}^{1+\varepsilon'}[0, 2\pi]$ ,  $0 < \varepsilon' < \varepsilon$ .*

Unfortunately, for the first method the computation of  $F$  requires a solution of a direct problem. In particular, if the curve  $\Gamma$  is the boundary of a domain with Jones frequency or close to such a boundary, the direct solution by finite elements is not easy. One way would be to compute with slightly modified frequencies. However, it might be difficult to

check whether the curve is “close” to the boundary of a domain with Jones frequency and to choose a modified frequency appropriately.

In order to motivate the second numerical method, the Kirsch-Kress algorithm, which corresponds to a third optimization problem, we introduce a second intermediate optimization method first. The plan is to define a method, where a solution of the direct method is not needed. Therefore, besides the unknown curve  $\Gamma$  the pressure  $p^s$  and the displacement field  $u$  are included into the set of optimization “parameters”. Additionally to the term of the least squares deviation of  $\mathcal{F}[p^s]$  from  $p_{noisy}^\infty$ , new terms are needed which enforce the fulfillment of the equations (2.1), (2.6), (2.4), (2.5), and (2.7) at least approximately. Hence, the regularized second optimization problem is to find a minimizer  $(\mathbf{r}_{min}, u_{min}, p_{min})$  of

$$\begin{aligned} & \inf_{\mathbf{r} \in H_{per}^{2+\varepsilon}[0, 2\pi], u \in [H^1(\Omega)]^2, p^s \in H^1(\Omega_R)} \mathcal{J}_\gamma^2(\mathbf{r}, u, p^s), \tag{3.4} \\ \mathcal{J}_\gamma^2(\mathbf{r}, u, p^s) & := \left\| \mathcal{F}[p^s] - p_{noisy}^\infty \right\|_{L^2[0, 2\pi]}^2 + \left\| \Delta^* u + \varrho \omega^2 u \right\|_{[H^{-1}(\Omega)]^2}^2 + \\ & \left\| \Delta p^s + k_w^2 p^s \right\|_{H^{-1}(\Omega_R)}^2 + \left\| t[u] + \{p^s + p^{inc}\} \nu \right\|_{[H^{-1/2}(\Gamma)]^2}^2 + \\ & \left\| u \cdot \nu - \frac{1}{\varrho_f \omega^2} \left\{ \frac{\partial p^s}{\partial \nu} + \frac{\partial p^{inc}}{\partial \nu} \right\} \right\|_{H^{-1/2}(\Gamma)}^2 + \\ & \left\| V_{\Gamma_0}^{ac}[\partial_\nu p^s] + \frac{1}{2}[p^s] - K_{\Gamma_0}^{ac}[p^s] \right\|_{H^{1/2}(\Gamma_0)}^2 + \\ & \gamma \|\mathbf{r}\|_{H_{per}^{2+\varepsilon}[0, 2\pi]}^2 + \gamma \|u\|_{H^1(\Omega)}^2 + \gamma \|p^s\|_{H^1(\Omega_R)}^2, \end{aligned}$$

where  $\gamma$  is a small positive regularization parameter. Of course, this is a theoretical optimization problem only. For a numerical realization, the operators should be replaced by those of the variational formulation (2.9). However, it is clearly seen that the price for avoiding a solution of the direct problem is an increase in the number of the optimization “parameters”. The numerical solution of the discretized optimization problem (3.4) is higher dimensional and might be more involved than that for the case of (3.2).

The third optimization problem is a modification of (3.4). The optimization “parameters”  $u$  and  $p^s$  are replaced by the layer functions  $\varphi_i$  and  $\vec{\varphi}_e$  of the potential representations (2.11). In other words, in the numerical discretization the finite elements over the domains  $\Omega$  and  $\Omega_R$  are replaced by lower dimensional boundary elements over the curves  $\Gamma_i$  and  $\Gamma_e$ . Instead of the terms in  $\mathcal{J}_\gamma^2$  enforcing the conditions (2.1), (2.6), (2.4), (2.5), and (2.7), we only need terms enforcing (2.14) and (2.15). Hence, the regularized third optimization problem is to find a minimizer  $(\mathbf{r}_{min}, \varphi_{i,min}, \vec{\varphi}_{e,min})$  of

$$\begin{aligned} & \inf_{\mathbf{r} \in H_{per}^{2+\varepsilon}[0, 2\pi], \varphi_i \in H^{-1}(\Gamma_i), \vec{\varphi}_e \in [H^{-1}(\Gamma_e)]^2} \mathcal{J}_\gamma^3(\mathbf{r}, \varphi_i, \vec{\varphi}_e), \tag{3.5} \\ \mathcal{J}_\gamma^3(\mathbf{r}, \varphi_i, \vec{\varphi}_e) & := c \left\| \mathcal{F}[V_{\Gamma_i}^{ac} \varphi_i] - p_{noisy}^\infty \right\|_{L^2[0, 2\pi]}^2 + \gamma \|\varphi_i\|_{H^{-1}(\Gamma_i)}^2 + \gamma \|\vec{\varphi}_e\|_{[H^{-1}(\Gamma_e)]^2}^2 + \\ & \left\| t[V_{\Gamma_e}^{el} \vec{\varphi}_e] + [V_{\Gamma_i}^{ac} \varphi_i] \nu + p^{inc} \nu \right\|_{L^2(\Gamma_r)}^2 + \left\| \varrho_f \omega^2 \nu \cdot [V_{\Gamma_i}^{el} \vec{\varphi}_e] - \partial_\nu [V_{\Gamma_i}^{ac} \varphi_i] - \partial_\nu p^{inc} \right\|_{L^2(\Gamma_r)}^2, \end{aligned}$$

where  $\gamma$  is a small positive regularization parameter and  $c$  a positive calibration constant. We choose the layers  $\varphi_{i,min}$  and  $\vec{\varphi}_{e,min}$  in an unusual Sobolev space of negative order to enable approximations by Dirac-delta functionals, i.e., by the method of fundamental

solutions. Though the number of optimization parameters in a discretization of (3.5) is larger than that in a discretization of (3.2), the objective functional  $\mathcal{J}_\gamma^3$  is simpler than  $\mathcal{J}_\gamma^1$ . Applying an optimization scheme like the conjugate gradient method or the Levenberg-Marquardt algorithm to (3.5), we arrive at the Kirsch-Kress method. Note that the accuracy of the solution of this method is limited by the accuracy of solving the integral equations (2.14) and (2.15) with a Tikhonov regularization. To improve this, the curves  $\Gamma_i$  and  $\Gamma_e$  can be updated during the iterative solution of the optimization problem (compare the iterative schemes in [14]).

**Theorem 3.2 ([5])** *Suppose  $k_\omega^2$  is not a Dirichlet eigenvalue for the negative Laplacian in the interior of  $\Gamma_i$  and that  $p^\infty$  is the exact far-field pattern of a scattered field  $p^s$  corresponding to some  $\Gamma^*$ . Then we have:*

- i) For any  $\gamma > 0$ , there is a unique minimizer  $(\mathbf{r}^\gamma, \varphi_i^\gamma, \vec{\varphi}_e^\gamma)$  of (3.5).*
- ii) Suppose  $(\mathbf{r}^\gamma, \varphi_i^\gamma, \vec{\varphi}_e^\gamma)$  is a set of minimizers for (3.5). Then the minima of the functionals, the  $\mathcal{J}_\gamma^3(\mathbf{r}^\gamma, \varphi_i^\gamma, \vec{\varphi}_e^\gamma)$ , tend to zero for  $\gamma \rightarrow 0$ .*
- iii) For any set of minimizers  $(\mathbf{r}^\gamma, \varphi_i^\gamma, \vec{\varphi}_e^\gamma)$ , there exists a subsequence  $(\mathbf{r}^{\gamma_n}, \varphi_i^{\gamma_n}, \vec{\varphi}_e^{\gamma_n})$  such that  $\mathbf{r}^{\gamma_n}$  converges weakly in  $H_{per}^{1+\varepsilon}[0, 2\pi]$  and strongly in  $H_{per}^{1+\varepsilon'}[0, 2\pi]$ ,  $0 < \varepsilon' < \varepsilon$ , to a solution  $\mathbf{r}^{**}$  of the inverse problem.*
- iv) If, additionally, the solution  $\mathbf{r}^*$  of the inverse problem is unique, then we even get that  $\mathbf{r}^\gamma$  tends to  $\mathbf{r}^*$  weakly in  $H_{per}^{1+\varepsilon}[0, 2\pi]$  and strongly in  $H_{per}^{1+\varepsilon'}[0, 2\pi]$ ,  $0 < \varepsilon' < \varepsilon$ .*

A discretization of the optimization problem (3.5) is presented in Section 6.3.

## 4 Some details of the implementation

For the solution of the optimization problems, a lot of **numerical optimization schemes** are available (cf. [17]). Unfortunately, global methods which yield the global minimum are often very slow. We recommend gradient based local optimization schemes. They provide local minimizers, i.e. solutions with minimal value of the objective functional in a neighbourhood of the minimizer. In general, it cannot be guaranteed that the local minimizer is the global minimizer. However, using a good initial guess, the local minimizer will coincide with the global. In particular, we have tested the Gauss-Newton method, the Levenberg-Marquardt algorithm (cf. [13]), and the conjugate gradient method. The last method has been tested for the Kirsch-Kress method to avoid the solution of linear systems in the size of the direct problem.

In order to compute **derivatives** of the objective functionals in case of the simple Newton iteration the calculus of shape derivatives can be applied. The derivatives result from solving the finite element system of the direct problem with new right-hand side vectors. This is fast if the finite element system is solved by an LU factorization for sparse systems (cf. [18, 4]). The derivatives for the Kirsch-Kress method can be obtained by a simple differentiation of the kernel functions in the potential representations. Since the elasticity kernel contains second-order derivatives of the acoustic kernel and since the terms enforcing the transmission conditions contain first-order derivatives of the elastic potential, we

need fourth order derivatives of the acoustic kernel. We present the needed formulas in Section 6.

Normally, **quadrature** rules are needed if the layer functions  $\varphi_i$  and  $\vec{\varphi}_e$  in the potential representation (2.11) are approximated by functions of a finite dimensional space. The potential integrals of these functions must be approximated by appropriate quadratures. However, in the case of the Kirsch-Kress method we can approximate the layer functions by linear combinations of Dirac delta functions

$$\varphi_i \sim \varphi_{i,M} := \sum_{\kappa=1}^M b_\kappa \delta_{x_{i,\kappa}}, \quad b_\kappa \in \mathbb{C}, \quad x_{i,\kappa} := r_i e^{it_\kappa}, \quad t_\kappa := \frac{2\pi\kappa}{M}, \quad (4.1)$$

$$\vec{\varphi}_e \sim \vec{\varphi}_{e,M} := \sum_{\kappa=1}^M c_\kappa \delta_{x_{e,\kappa}}, \quad c_\kappa \in \mathbb{C}^2, \quad x_{e,\kappa} := r_e e^{it_\kappa}. \quad (4.2)$$

This works since the potential operators are smoothing operators from the curve  $\Gamma_e, \Gamma_i$  to  $\Gamma$ . Only in the case that  $\Gamma_e$  or  $\Gamma_i$  is close to  $\Gamma$ , a trigonometric or spline approximation of  $\varphi_i$  and  $\vec{\varphi}_e$  together with an accurate quadrature must be employed.

Another important issue is the **scaling** of the optimization scheme. Indeed, the number of necessary iterations depends on the conditioning of the optimization problem. Using an appropriate scaling, the conditioning can be essentially improved. The first choice is, of course, the natural scaling. The far-field values should be scaled such that the measurement uncertainties of the scaled far-field values coincide, and the parameters should be scaled in accordance with the accuracy requirements. A scaling different from the natural one is chosen not to improve the reconstruction operator, but to speed up the optimization algorithm. This calibration may include different constants in front of the individual terms in the objective functional (cf. the factors  $c$  and  $\gamma$  in the definition of  $\mathcal{J}_\gamma^3$ ) and the replacement of the optimization parameters by the products of these parameters with convenient constants. The constants can be chosen, e.g., to minimize the conditioning of the Jacobian of the mapping that maps the parameters to the far-field values. Alternatively, the constants can be chosen by checking typical test examples with known solution. To improve the conditioning of the optimization in the Kirsch-Kress method, we have replaced the ‘‘optimization parameters’’  $\mathbf{r}$ ,  $\varphi_i$ , and  $\vec{\varphi}_e$  by the parameters

$$\mathbf{r}' = \mathbf{r}/c_r, \quad \varphi_i' = \varphi_i/c_i, \quad \vec{\varphi}_e' = \vec{\varphi}_e/c_e. \quad (4.3)$$

## 5 Numerical results

We have employed i) the simple Newton iteration and ii) the Kirsch-Kress method, both with a circle as initial solution, to reconstruct two different obstacles. The first is an easy egg shaped domain (cf. Figure 9) with a boundary given by (3.1), by  $r_i = 2$ ,  $r_e = 6$ , and by the fast decaying Fourier coefficients

$$\begin{aligned} \hat{a}_0 &= 0, \\ \hat{a}_1 &= -1, \quad \hat{a}_2 = 0.1, \quad \hat{a}_3 = 0.01, \quad \hat{a}_4 = -0.001, \quad \hat{a}_5 = 0.0001, \\ \hat{b}_1 &= 1, \quad \hat{b}_2 = 0.1, \quad \hat{b}_3 = 0.01, \quad \hat{b}_4 = 0.001, \quad \hat{b}_5 = 0.0001. \end{aligned} \quad (5.1)$$

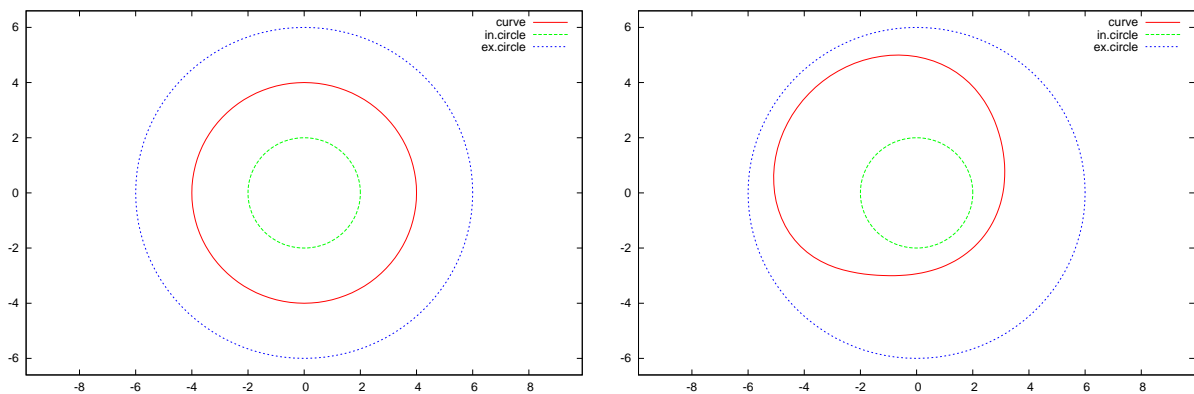


Figure 9: Initial solution and egg shaped domain.

The second body is the nonconvex obstacle from the end of Section 2 (cf. Figure 10), and its boundary is given by  $r_i = 2$ ,  $r_e = 6$  and by the Fourier coefficients

$$\begin{aligned}
 \hat{a}_0 &= 0, \\
 \hat{a}_1 &= 1, \quad \hat{a}_2 = 0.10, \quad \hat{a}_3 = 0.040, \quad \hat{a}_4 = 0.016, \quad \hat{a}_5 = 0.008, \\
 \hat{b}_1 &= -1, \quad \hat{b}_2 = 0.02, \quad \hat{b}_3 = -1.500, \quad \hat{b}_4 = -0.010, \quad \hat{b}_5 = 0.008.
 \end{aligned} \tag{5.2}$$

In all computations, we have chosen the physical constants in accordance with (2.17). The incoming plane wave has been fixed to  $p^{inc}(x) := e^{i(1,0)^\top \cdot x}$ . Moreover, for all initial curves and all iterative solutions, we have fixed the zeroth Fourier coefficient  $\hat{a}_0$  to zero. The “measured” far-field data  $\{p^\infty(k/M''), k = 1, \dots, M''\}$ ,  $M'' = 80$  (cf. Figure 8) has been simulated by the piecewise linear finite element method (FEM) described in Section 2. To avoid what is called an inverse crime, we have chosen the meshsize of the FEM grid (determined by NETGEN [19]) for the far-field computation by a factor of at least 0.25 smaller than that of the FEM grids involved in the inverse algorithms. Our tests have revealed that the far-field of the FEM method is more reliable than that computed by the regularized system (2.14)-(2.15). The scaling parameters  $c$ ,  $c_r$ ,  $c_i$ , and  $c_e$  for the Kirsch-Kress method (cf. (4.3) and the definition of  $\mathcal{J}_\gamma^3$ ) have been determined experimentally such that the reconstruction by Gauss-Newton iteration converges with the smallest number of iteration steps. For example, for the egg shaped domain and  $M=M'=44$  points of discretization for the approximate integration over  $\Gamma$ ,  $\Gamma_i$ ,  $\Gamma_e$  (cf. the discretized objective functional in (6.5)), these values are  $c = 4000$ ,  $c_r = 1$ ,  $c_i = 0.1$ , and  $c_e = 0.005$ .

The results for the egg shaped domain and for the simple Newton iteration have been similar to those presented in [4], where the constants were slightly different and the obstacle was similar to our nonconvex body. After a small number ( $\leq 20$ ) of iterations, the algorithm reconstructs the obstacle. The regularization parameter  $\gamma$  can even be set to zero, which is not surprising since only 10 unknown real parameters are reconstructed from 160 real measurement values. Table 1 exhibits the meshsize  $h$ , the number of Gauss-Newton iterations  $it$ , and the accuracy  $err := \|\tilde{\mathbf{r}} - \tilde{\mathbf{r}}_{FEM}\|_{L^\infty[0,2\pi]}$  of the reconstruction  $\mathbf{r}_{FEM}$ . The results for the nonconvex obstacle are similar (cf. Table 2). Most of the computing time is spent on the evaluation of the objective functional including the solution



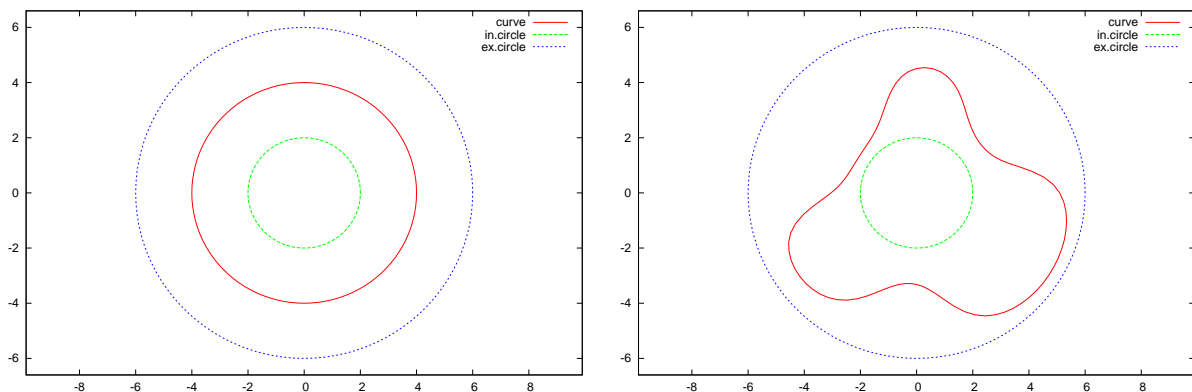


Figure 10: Initial solution and nonconvex domain.

of a direct problem. Therefore, it is not necessary to replace the expensive Gauss-Newton iteration by a different optimization scheme.

We have started the tests of the Kirsch-Kress method with the nonconvex domain. However, the optimization algorithms did not converge. To fix the problem, we have checked the solution of the corresponding direct problem. We have observed that the far-field of the solution computed by (2.11), (2.14), and (2.15) did not match that of the FEM. Even a Tikhonov regularization in accordance with the last four terms of the functional  $\mathcal{J}_\gamma^3$  did not help. Only a regularization with a truncated singular value decomposition and a well-chosen truncation parameter led to the correct far field. In other words, the reason for the divergence of the Kirsch-Kress method is the high degree of ill-posedness of the system (2.14),(2.15). On the other hand, if we commit the inverse crime and take the incorrect far-field data computed by solving (2.14),(2.15), then the Kirsch-Kress algorithm does converge.

To show the convergence of the Kirsch-Kress method with FEM generated far-field data, we consider the egg shaped domain. This time the solution curve has a higher degree of smoothness, and the direct solution of (2.14),(2.15) together with a Tikhonov regularization yields a far-field solution close to that of the FEM. Table 3 shows that the Kirsch-Kress method converges for the egg shaped domain. Indeed, the table shows the regularization parameter  $\gamma$ , the error  $\|\tilde{\mathbf{r}} - \tilde{\mathbf{r}}_{KK}\|_{L_p^\infty er[0,2\pi]}$  of the Kirsch-Kress reconstruction  $\mathbf{r}_{KK}$ , and the number of necessary iteration steps. These depend on the number

| $h$     | $err$   | $it$ |
|---------|---------|------|
| 0.5     | 0.0759  | 6    |
| 0.25    | 0.0247  | 8    |
| 0.125   | 0.00876 | 8    |
| 0.0625  | 0.00329 | 10   |
| 0.03125 | 0.00156 | 10   |

Table 1: Reconstruction of egg shaped domain by simple Newton iteration.



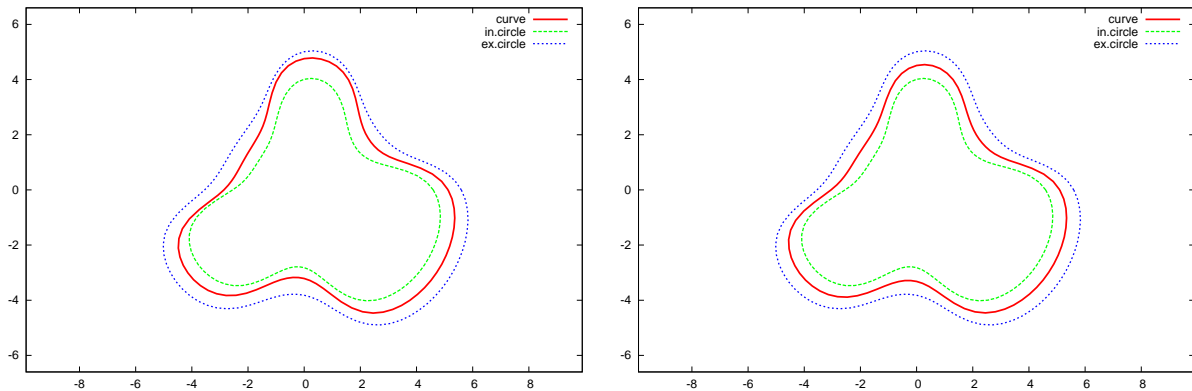


Figure 11: Initial solution with Fourier coefficients  $\hat{a}_i^1, \hat{b}_i^1$  and nonconvex domain with modified curves  $\Gamma_i$  and  $\Gamma_e$ .

of discretization points  $M = M'$  for the approximate integration over  $\Gamma, \Gamma_i, \Gamma_e$  (cf. the discretized objective functional in (6.5)) and on the choice of the optimization method. In particular, we have checked the Gauss-Newton method with experimentally chosen regularization parameter  $\gamma$  (GNw), the Levenberg-Marquardt method with the same regularization parameter (LMw), and the Levenberg-Marquardt method without regularization (LMo). The results show much better approximations than for the simple Newton iteration. Unfortunately, the conjugate gradient method did not converge.

To get convergence of the Kirsch-Kress method also for the nonconvex domain of Figure 10, we have changed the curves  $\Gamma_i$  and  $\Gamma_e$  (cf. Figure 11). If these are closer to the curve  $\Gamma^r$ , then the degree of ill-posedness of the operators in (2.14),(2.15) is reduced. We have chosen the initial guess of the Fourier coefficients as

$$\begin{aligned} \hat{a}_0^0 &= 0.0, \\ \hat{a}_1^0 &= 1.3, \quad \hat{a}_2^0 = -0.10, \quad \hat{a}_3^0 = 0.1, \quad \hat{a}_4^0 = -0.05, \quad \hat{a}_5^0 = 0.018, \\ \hat{b}_1^0 &= -0.8, \quad \hat{b}_2^0 = 0.05, \quad \hat{b}_3^0 = -1.7, \quad \hat{b}_4^0 = 0.03, \quad \hat{b}_5^0 = -0.020. \end{aligned} \quad (5.3)$$

Since the iteration, with this initial solution, converged to a false local minimum, we have introduced an initial solution closer to the true solution in (5.2). We have checked the initial solution

$$\hat{a}_i^1 := \frac{1}{2}(\hat{a}_i^0 + \hat{a}_i), \quad i = 0, \dots, 5, \quad \hat{b}_i^1 := \frac{1}{2}(\hat{b}_i^0 + \hat{b}_i), \quad i = 1, \dots, 5$$

| $h$     | $err$   | $it$ |
|---------|---------|------|
| 0.25    | 1.1435  | 20   |
| 0.125   | 0.00924 | 17   |
| 0.0625  | 0.00401 | 15   |
| 0.03125 | 0.00157 | 18   |

Table 2: Reconstruction of nonconvex domain by simple Newton iteration.

and observed convergence. In particular, we had to choose a larger number of discretization points on the curves  $\Gamma$ ,  $\Gamma_i$ ,  $\Gamma_e$ , namely  $M = M' = 352$ . We have set the regularization parameter  $\gamma = 10^{-8}$  and the scaling constants to  $c = 10\,000$ ,  $c_r = 1$ ,  $c_i = 1$ , and  $c_e = 0.2$ . For the initial solution  $\{\hat{a}_i^1, \hat{b}_i^1\}$ , we got the reconstructed curve within 11 iterations of the Gauss-Newton method. The error  $\|\tilde{\mathbf{r}} - \tilde{\mathbf{r}}_{ini}\|_{L^\infty[0,2\pi]} = 0.296$  of the initial parametrization  $\mathbf{r}_{ini}$  with Fourier coefficients  $\hat{a}_i^1, \hat{b}_i^1$  has been reduced to  $\|\tilde{\mathbf{r}} - \tilde{\mathbf{r}}_{KK}\|_{L^\infty[0,2\pi]} = 0.000279$ .

Finally, we have checked perturbed far-field data. For different values of  $\varepsilon$ , we have added a random number, uniformly distributed in  $[-\varepsilon, \varepsilon]$ , to the far-field values of the egg shaped domain. Tables 4 and 5 show the reconstruction accuracy depending on  $\varepsilon$  for the simple Newton iteration with FEM stepsize 0.03125 and for the Kirsch-Kress method with a number of discretization points  $M = M' = 44$ , respectively. Obviously, the simple Newton iteration is much more robust with respect to random perturbations. For the Kirsch-Kress method with  $M = M' = 352$  points applied to the nonconvex domain (cf. Figure 11), the test results are shown in Table 6.

Summarizing the results, the advantage of the Kirsch-Kress method is the high accuracy of reconstruction. Since methods like the conjugate gradient algorithm do not necessarily converge, we cannot claim that, using the Kirsch-Kress method, the solution of large linear systems in the size of the matrices of the direct methods can be avoided. The disadvantage of the Kirsch-Kress method is that small measurement uncertainties of the far-field data, high degrees of ill-posedness, and bad scalings can lead to divergent iterations.

| number of points $M = M'$ | $\gamma$              | GNw            | LMw            | LMo             |
|---------------------------|-----------------------|----------------|----------------|-----------------|
| 22                        | $4 \cdot 10^{-8}$     | 0.05427 (13)   | 0.05461 (30)   | 0.06793 (30)    |
| 44                        | $0.25 \cdot 10^{-12}$ | 0.002136 (13)  | 0.002007 (320) | 0.002095 (320)  |
| 88                        | $4 \cdot 10^{-14}$    | 0.0002126 (13) | 0.0002107 (80) | 0.0001997 (160) |

Table 3: Reconstruction accuracy (number of iterations) in dependence on the optimization method and on the number of discretization points for the egg shaped domain.

| $\varepsilon$ | $\ \tilde{\mathbf{r}} - \tilde{\mathbf{r}}_{FEM}\ _{L^\infty}$ |
|---------------|--|
| 0.            | 0.001568   |
| 0.001         | 0.002637   |
| 0.005         | 0.007156   |
| 0.01          | 0.01368  |
| 0.05          | 0.05433  |
| 0.1           | 0.1087   |
| 0.2           | 0.2339   |

Table 4: Reconstruction error of the simple Newton iteration depending on the stochastic perturbation of the far-field data, egg shaped domain, regularization parameter  $\gamma=0$ .

| $\varepsilon$ | $\gamma$              | $\ \tilde{\mathbf{r}} - \tilde{\mathbf{r}}_{KK}\ _{L^\infty}$ |
|---------------|-----------------------|---|
| 0.            | $0.25 \cdot 10^{-12}$ | 0.002136  |
| 0.0001        | $0.25 \cdot 10^{-10}$ | 0.003640  |
| 0.001         | $0.25 \cdot 10^{-7}$  | 0.02041   |
| 0.003         | $0.25 \cdot 10^{-6}$  | 0.05686   |
| 0.005         | $1 \cdot 10^{-6}$     | 0.09997   |

Table 5: Reconstruction error of the Kirsch-Kress method depending on the stochastic perturbation of the far-field data, egg shaped domain.

| $\varepsilon$ | $\gamma$  | $\ \tilde{\mathbf{r}} - \tilde{\mathbf{r}}_{KK}\ _{L^\infty}$ | $it$ |
|---------------|-----------|---|------|
| 0.00000       | $10^{-8}$ | 0.00028   | 11   |
| 0.00010       | $10^{-8}$ | 0.0141  | 13   |
| 0.00025       | $10^{-8}$ | 0.0345  | 11   |
| 0.00100       | $10^{-8}$ | 0.113   | 8    |
| 0.00250       | $10^{-6}$ | 0.187   | 9    |

Table 6: Reconstruction error of the Kirsch-Kress method depending on the stochastic perturbation of the far-field data, nonconvex domain.

## 6 Appendix:

### Derivatives of the 2D discretized objective functional

#### 6.1 Derivatives of the points at the parameterized curve and of the normal vector with respect to $a$

Now we derive formulas for the parameterization point  $x_{\mathbf{r}}(\zeta) := \tilde{\mathbf{r}}(\zeta) \exp(i\zeta)$  (cf. 3.1) on the approximate interface, for the normal  $\nu$  at  $x_{\mathbf{r},\kappa}$ , and for their derivatives with respect to the Fourier coefficients. Clearly, the set of coefficients is to be truncated such that we can compute with a finite set of parameters  $\{\hat{a}_0, \hat{a}_j, \hat{b}_j : j = 1, 2, \dots, n\}$ . To simplify the formulas, we set  $N = 2n + 1$  and collect these Fourier coefficients in the set  $\{a_\iota : \iota \in I_N\}$  and write the parametric representation as

$$x_{\mathbf{r}}(\zeta) := \mathbf{r}(\zeta) e^{i\zeta}, \quad \mathbf{r}(\zeta) := \frac{r_{e+r_i}}{2} + \frac{r_{e-r_i}}{\pi} \arctan\left(\sum_{\iota \in I_N} a_\iota \psi_\iota(\zeta)\right). \quad (6.1)$$

Here  $\psi_\iota(\zeta) = \cos(j\zeta)$  if  $a_\iota = \hat{a}_j$  and  $\psi_\iota(\zeta) = \sin(j\zeta)$  if  $a_\iota = \hat{b}_j$ . For the derivatives, we arrive at

$$\begin{aligned} \mathbf{r}'(\zeta) &= \frac{r_{e-r_i}}{\pi} \frac{\sum_{\iota \in I_N} a_\iota \psi'_\iota(\zeta)}{1 + \left(\sum_{\iota \in I_N} a_\iota \psi_\iota(\zeta)\right)^2}, \\ \frac{\partial}{\partial a_\iota} \mathbf{r}(\zeta) &= \frac{r_{e-r_i}}{\pi} \frac{\psi_\iota(\zeta)}{1 + \left(\sum_{\iota' \in I_N} a_{\iota'} \psi_{\iota'}(\zeta)\right)^2}, \\ \frac{\partial}{\partial a_\iota} x_{\mathbf{r}}(\zeta) &= \frac{r_{e-r_i}}{\pi} \frac{\psi_\iota(\zeta)}{1 + \left(\sum_{\iota' \in I_N} a_{\iota'} \psi_{\iota'}(\zeta)\right)^2} e^{i\zeta}, \\ \frac{\partial}{\partial a_\iota} \mathbf{r}'(\zeta) &= \frac{r_{e-r_i}}{\pi} \frac{\psi'_\iota(\zeta)}{1 + \left(\sum_{\iota' \in I_N} a_{\iota'} \psi_{\iota'}(\zeta)\right)^2} \\ &\quad - 2 \frac{r_{e-r_i}}{\pi} \frac{\left[\sum_{\iota' \in I_N} a_{\iota'} \psi'_{\iota'}(\zeta)\right] \left[\sum_{\iota' \in I_N} a_{\iota'} \psi_{\iota'}(\zeta)\right] \psi_\iota(\zeta)}{\left[1 + \left(\sum_{\iota' \in I_N} a_{\iota'} \psi_{\iota'}(\zeta)\right)^2\right]^2}. \end{aligned}$$

A normal  $\tilde{\nu}$  to the curve at  $x_{\mathbf{r}}(\zeta)$  and the unit normal  $\nu$  are given by

$$\begin{aligned} \tilde{\nu}(x_{\mathbf{r}}(\zeta)) &= e^{-i\pi/2} \frac{\partial}{\partial \zeta} [x_{\mathbf{r}}(\zeta)] = e^{-i\pi/2} \frac{\partial}{\partial \zeta} [\mathbf{r}(\zeta) e^{i\zeta}] \\ &= e^{-i\pi/2} [\mathbf{r}'(\zeta) e^{i\zeta} + \mathbf{r}(\zeta) e^{i\pi/2} e^{i\zeta}] = [e^{-i\pi/2} \mathbf{r}'(\zeta) + \mathbf{r}(\zeta)] e^{i\zeta}, \\ \nu(x_{\mathbf{r}}(\zeta)) &= \frac{[e^{-i\pi/2} \mathbf{r}'(\zeta) + \mathbf{r}(\zeta)] e^{i\zeta}}{|e^{-i\pi/2} \mathbf{r}'(\zeta) + \mathbf{r}(\zeta)|} = \frac{\mathbf{r}'(\zeta) e^{i(\zeta-\pi/2)} + \mathbf{r}(\zeta) e^{i\zeta}}{\sqrt{\mathbf{r}'(\zeta)^2 + \mathbf{r}(\zeta)^2}}. \end{aligned} \quad (6.2)$$

The derivatives of these entities can be computed by the formulas

$$\begin{aligned}
\frac{\partial}{\partial a_l} \nu(x_{\mathbf{r}}(\zeta)) &= \frac{\partial}{\partial a_l} \frac{\mathbf{r}'(\zeta)}{\sqrt{\mathbf{r}'(\zeta)^2 + \mathbf{r}(\zeta)^2}} e^{i(\zeta - \pi/2)} + \frac{\partial}{\partial a_l} \frac{\mathbf{r}(\zeta)}{\sqrt{\mathbf{r}'(\zeta)^2 + \mathbf{r}(\zeta)^2}} e^{i\zeta}, \\
\frac{\partial}{\partial a_l} \frac{\mathbf{r}'(\zeta)}{\sqrt{\mathbf{r}'(\zeta)^2 + \mathbf{r}(\zeta)^2}} &= \frac{\partial_{a_l} \mathbf{r}'(\zeta)}{\sqrt{\mathbf{r}'(\zeta)^2 + \mathbf{r}(\zeta)^2}} - \frac{1}{2} \frac{\mathbf{r}'(\zeta) \{2\mathbf{r}'(\zeta) \partial_{a_l} \mathbf{r}'(\zeta) + 2\mathbf{r}(\zeta) \partial_{a_l} \mathbf{r}(\zeta)\}}{\sqrt{\mathbf{r}'(\zeta)^2 + \mathbf{r}(\zeta)^2}^3} \\
&= \frac{\partial_{a_l} \mathbf{r}'(\zeta)}{\sqrt{\mathbf{r}'(\zeta)^2 + \mathbf{r}(\zeta)^2}} - \frac{\mathbf{r}'(\zeta) \{\mathbf{r}'(\zeta) \partial_{a_l} \mathbf{r}'(\zeta) + \mathbf{r}(\zeta) \partial_{a_l} \mathbf{r}(\zeta)\}}{\sqrt{\mathbf{r}'(\zeta)^2 + \mathbf{r}(\zeta)^2}^3}, \\
\frac{\partial}{\partial a_l} \frac{\mathbf{r}(\zeta)}{\sqrt{\mathbf{r}'(\zeta)^2 + \mathbf{r}(\zeta)^2}} &= \frac{\partial_{a_l} \mathbf{r}(\zeta)}{\sqrt{\mathbf{r}'(\zeta)^2 + \mathbf{r}(\zeta)^2}} - \frac{\mathbf{r}(\zeta) \{\mathbf{r}'(\zeta) \partial_{a_l} \mathbf{r}'(\zeta) + \mathbf{r}(\zeta) \partial_{a_l} \mathbf{r}(\zeta)\}}{\sqrt{\mathbf{r}'(\zeta)^2 + \mathbf{r}(\zeta)^2}^3}.
\end{aligned}$$

## 6.2 Values and derivatives of incoming wave and kernel functions

Suppose  $v^{inc}$  is the direction of the incoming wave, then

$$\begin{aligned}
p^{inc}(x) &= e^{\mathbf{i}k_\omega v^{inc} \cdot x}, \\
\partial_{x_j} p^{inc}(x) &= \mathbf{i}k_\omega e^{\mathbf{i}k_\omega v^{inc} \cdot x} [v^{inc}]_j, \\
\partial_{x_j} \partial_{x_l} p^{inc}(x) &= -k_\omega^2 e^{\mathbf{i}k_\omega v^{inc} \cdot x} [v^{inc}]_j [v^{inc}]_l.
\end{aligned}$$

For the derivatives of the acoustic Green kernel, we obtain (cf. [1])

$$\begin{aligned}
G(x, y) &= \frac{\mathbf{i}}{4} H_0^{(1)}(k|x - y|), & H_0^{(1)}(t) &:= J_0(t) + \mathbf{i}Y_0(t), \\
\partial_{x_j} G(x, y) &= \frac{\mathbf{i}k}{4} [H_0^{(1)}]'(k|x - y|) \frac{(x_j - y_j)}{|x - y|}, & [H_0^{(1)}]'(t) &:= -J_1(t) - \mathbf{i}Y_1(t), \\
\partial_{y_j} G(x, y) &= \frac{\mathbf{i}k}{4} [H_0^{(1)}]'(k|x - y|) \frac{(y_j - x_j)}{|x - y|}, \\
\partial_{x_j} \partial_{x_l} G(x, y) &= \frac{\mathbf{i}k}{4} [H_0^{(1)}]'(k|x - y|) \frac{|x - y|^2 \delta_{j,l} - 2(x_j - y_j)(x_l - y_l)}{|x - y|^3} \\
&\quad - \frac{\mathbf{i}k^2}{4} H_0^{(1)}(k|x - y|) \frac{(x_j - y_j)(x_l - y_l)}{|x - y|^2}.
\end{aligned}$$

For the third order derivatives, we observe

$$\begin{aligned}
\partial_{x_m} \partial_{x_j} \partial_{x_l} G(x, y) &= \mathbf{i}k^2 H_0^{(1)}(k|x - y|) \left\{ \frac{(x_j - y_j)(x_l - y_l)(x_m - y_m)}{|x - y|^4} \right. \\
&\quad \left. - \frac{(x_m - y_m)\delta_{j,l} + (x_l - y_l)\delta_{j,m} + (x_j - y_j)\delta_{l,m}}{4|x - y|^2} \right\} \\
&\quad + \frac{\mathbf{i}k}{2} [H_0^{(1)}]'(k|x - y|) \left\{ \frac{(x_m - y_m)(x_j - y_j)(x_l - y_l)}{2|x - y|^5} [8 - k^2|x - y|^2] \right. \\
&\quad \left. - \frac{(x_m - y_m)\delta_{j,l} + (x_l - y_l)\delta_{j,m} + (x_j - y_j)\delta_{l,m}}{|x - y|^3} \right\}
\end{aligned}$$

$$\begin{aligned}
\partial_{y_m} \partial_{x_j} \partial_{x_l} G(x, y) &= \mathbf{i} k^2 H_0^{(1)}(k|x-y|) \left\{ \frac{(y_j - x_j)(y_l - x_l)(y_m - x_m)}{|x-y|^4} \right. \\
&\quad \left. - \frac{(y_m - x_m)\delta_{j,l} + (y_l - x_l)\delta_{j,m} + (y_j - x_j)\delta_{l,m}}{4|x-y|^2} \right\} \\
&+ \frac{\mathbf{i}k}{2} [H_0^{(1)}]'(k|x-y|) \left\{ \frac{(y_m - x_m)(y_j - x_j)(y_l - x_l)}{2|x-y|^5} [8 - k^2|x-y|^2] \right. \\
&\quad \left. - \frac{(y_m - x_m)\delta_{j,l} + (y_l - x_l)\delta_{j,m} + (y_j - x_j)\delta_{l,m}}{|x-y|^3} \right\}.
\end{aligned}$$

The fourth order derivatives take the form

$$\begin{aligned}
\partial_{y_n} \partial_{y_m} \partial_{x_j} \partial_{x_l} G(x, y) &= \\
&\mathbf{i} k^2 H_0^{(1)}(k|x-y|) \left\{ \frac{(y_l - x_l)(y_m - x_m)\delta_{n,j}}{|x-y|^4} + \frac{(y_j - x_j)(y_m - x_m)\delta_{n,l}}{|x-y|^4} \right. \\
&\quad + \frac{(y_j - x_j)(y_l - x_l)\delta_{n,m}}{|x-y|^4} - \frac{\delta_{j,l}\delta_{n,m} + \delta_{j,m}\delta_{n,l} + \delta_{l,m}\delta_{n,j}}{4|x-y|^2} \\
&\quad + (y_n - x_n) \frac{(y_m - x_m)\delta_{j,l} + (y_l - x_l)\delta_{j,m} + (y_j - x_j)\delta_{l,m}}{|x-y|^4} \\
&\quad \left. - \frac{(y_n - x_n)(y_m - x_m)(y_j - x_j)(y_l - x_l)}{4|x-y|^6} [24 - k^2|x-y|^2] \right\} \\
&+ \mathbf{i} k [H_0^{(1)}]'(k|x-y|) \left\{ [2k^2|x-y|^2 - 12] \frac{(y_j - x_j)(y_l - x_l)(y_m - x_m)(y_n - x_n)}{|x-y|^7} \right. \\
&\quad + [8 - k^2|y-x|^2] \times \\
&\quad \quad \frac{(y_n - x_n)(y_m - x_m)\delta_{j,l} + (y_l - x_l)\delta_{j,m} + (y_j - x_j)\delta_{l,m}}{4|x-y|^5} \\
&\quad + [8 - k^2|x-y|^2] \times \\
&\quad \quad \frac{(y_j - x_j)(y_l - x_l)\delta_{n,m} + (y_m - x_m)(y_l - x_l)\delta_{n,j} + (y_m - x_m)(y_j - x_j)\delta_{n,l}}{4|x-y|^5} \\
&\quad \quad \left. - \frac{\delta_{j,l}\delta_{n,m} + \delta_{j,m}\delta_{n,l} + \delta_{l,m}\delta_{n,j}}{2|x-y|^3} \right\}.
\end{aligned}$$

For the derivatives of the elastic Green kernel, we conclude

$$\begin{aligned}
[G^{el}(x, y)]_{j,l} &= \frac{1}{\mu} G(x, y; k_s) \delta_{j,l} + \frac{1}{\mu k_s^2} \partial_{x_j} \partial_{x_l} G(x, y; k_s) - \frac{1}{\mu k_s^2} \partial_{x_j} \partial_{x_l} G(x, y; k_p), \\
\partial_{y_m} [G^{el}(x, y)]_{j,l} &= \frac{1}{\mu} \partial_{y_m} G(x, y; k_s) \delta_{j,l} + \frac{1}{\mu k_s^2} \partial_{y_m} \partial_{x_j} \partial_{x_l} G(x, y; k_s) \\
&\quad - \frac{1}{\mu k_s^2} \partial_{y_m} \partial_{x_j} \partial_{x_l} G(x, y; k_p),
\end{aligned}$$

$$\begin{aligned} \partial_{y_n} \partial_{y_m} [G^{el}(x, y)]_{j,l} &= \frac{1}{\mu} \partial_{y_n} \partial_{y_m} G(x, y; k_s) \delta_{j,l} + \frac{1}{\mu k_s^2} \partial_{y_n} \partial_{y_m} \partial_{x_j} \partial_{x_l} G(x, y; k_s) \\ &\quad - \frac{1}{\mu k_s^2} \partial_{y_n} \partial_{y_m} \partial_{x_j} \partial_{x_l} G(x, y; k_p), \end{aligned}$$

$$\begin{aligned} t_y [G^{el}(x, y)]_{\cdot,l} &= 2\mu \left( \begin{array}{c} \sum_{j=1}^2 \nu_j \partial_{y_j} [G^{el}(x, y)]_{1,l} \\ \sum_{j=1}^2 \nu_j \partial_{y_j} [G^{el}(x, y)]_{2,l} \end{array} \right) \\ &\quad + \lambda \left[ \partial_{y_1} [G^{el}(x, y)]_{1,l} + \partial_{y_2} [G^{el}(x, y)]_{2,l} \right] \nu \\ &\quad + \mu \left( \begin{array}{c} \nu_2 \left( \partial_{y_1} [G^{el}(x, y)]_{2,l} - \partial_{y_2} [G^{el}(x, y)]_{1,l} \right) \\ \nu_1 \left( \partial_{y_2} [G^{el}(x, y)]_{1,l} - \partial_{y_1} [G^{el}(x, y)]_{2,l} \right) \end{array} \right), \end{aligned}$$

$$\begin{aligned} \partial_{y_m} t_y [G^{el}(x, y)]_{\cdot,l} &= 2\mu \left( \begin{array}{c} \sum_{j=1}^2 \nu_j \partial_{y_m} \partial_{y_j} [G^{el}(x, y)]_{1,l} \\ \sum_{j=1}^2 \nu_j \partial_{y_m} \partial_{y_j} [G^{el}(x, y)]_{2,l} \end{array} \right) \\ &\quad + \lambda \left[ \partial_{y_m} \partial_{y_1} [G^{el}(x, y)]_{1,l} + \partial_{y_m} \partial_{y_2} [G^{el}(x, y)]_{2,l} \right] \nu \\ &\quad + \mu \left( \begin{array}{c} \nu_2 \left( \partial_{y_m} \partial_{y_1} [G^{el}(x, y)]_{2,l} - \partial_{y_m} \partial_{y_2} [G^{el}(x, y)]_{1,l} \right) \\ \nu_1 \left( \partial_{y_m} \partial_{y_2} [G^{el}(x, y)]_{1,l} - \partial_{y_m} \partial_{y_1} [G^{el}(x, y)]_{2,l} \right) \end{array} \right), \end{aligned}$$

$$\begin{aligned} \partial_{\nu_m} t_y [G^{el}(x, y)]_{\cdot,l} &= 2\mu \left( \begin{array}{c} \partial_{y_m} [G^{el}(x, y)]_{1,l} \\ \partial_{y_m} [G^{el}(x, y)]_{2,l} \end{array} \right) \\ &\quad + \lambda \left[ \partial_{y_1} [G^{el}(x, y)]_{1,l} + \partial_{y_2} [G^{el}(x, y)]_{2,l} \right] \begin{pmatrix} \delta_{1,m} \\ \delta_{2,m} \end{pmatrix} \\ &\quad + \mu \left( \begin{array}{c} \delta_{2,m} \left( \partial_{y_1} [G^{el}(x, y)]_{2,l} - \partial_{y_2} [G^{el}(x, y)]_{1,l} \right) \\ \delta_{1,m} \left( \partial_{y_2} [G^{el}(x, y)]_{1,l} - \partial_{y_1} [G^{el}(x, y)]_{2,l} \right) \end{array} \right). \end{aligned}$$

### 6.3 Least squares approach for the Gauss-Newton algorithm

Suppose  $I_N$  is the index set of the Fourier coefficients from Subsection 6.1 and the layer functions of the Kirsch-Kress method are approximated by (4.1), (4.2). Furthermore, suppose the  $L^2$  norms on  $\Gamma^{\mathbf{r}}$  and  $[0, 2\pi]$  in  $\mathcal{J}_\gamma^3$  are discretized by

$$\|f\|_{L^2(\Gamma^{\mathbf{r}})}^2 \sim \sum_{\kappa=1}^{M'} |f(x_{\mathbf{r},\kappa})|^2, \quad x_{\mathbf{r},\kappa} := \mathbf{r}(\tau_\kappa) e^{i\tau_\kappa}, \quad \tau_\kappa := \frac{2\pi\kappa}{M'}, \quad (6.3)$$

$$\|g\|_{L^2[0,2\pi]}^2 \sim \sum_{\kappa=1}^{M''} |g(\sigma_\kappa)|^2, \quad \sigma_\kappa := \frac{2\pi\kappa}{M''}, \quad (6.4)$$

Then the discretized objective functional for (3.5) is of the form

$$\begin{aligned} \mathcal{J}_{N,M,M',\gamma}(\varphi_{i,M}, \vec{\varphi}_{e,M}, \mathbf{r}_N) &:= \left\| \mathcal{M}\left((b_\kappa)_{\kappa=1}^M, (c_\kappa)_{\kappa=1}^M, (a_l)_{l \in I_N}\right) - \mathcal{R} \right\|_{\ell^2}^2, \\ \mathcal{M} &:= \left( (\mathcal{M}_{1,\kappa}), (\mathcal{M}_{2,\kappa}), (\mathcal{M}_{3,\kappa,l}), (\mathcal{M}_{4,\kappa,l}), (\mathcal{M}_{5,\kappa}) \right), \\ \mathcal{R} &:= \left( (\mathcal{R}_{1,\kappa}), (\mathcal{R}_{2,\kappa}), (\mathcal{R}_{3,\kappa,l}), (\mathcal{R}_{4,\kappa,l}), (\mathcal{R}_{5,\kappa}) \right), \end{aligned} \quad (6.5)$$

where

$$\begin{aligned} \mathcal{R}_{1,\kappa} &:= \frac{1}{\sqrt{M''}} p_{\text{noisy}}^\infty(\sigma_{\kappa'}), \\ \mathcal{R}_{2,\kappa'} &:= 0, \\ \mathcal{R}_{3,\kappa',l} &:= 0, \\ \mathcal{R}_{4,\kappa',l} &:= 0, \\ \mathcal{R}_{5,\kappa'} &:= 0, \end{aligned} \quad (6.6)$$

$$\begin{aligned} \mathcal{M}\left((b_\kappa), (c_\kappa), (a_l)\right)_{1,\kappa'} &:= \frac{e^{i\pi/4}}{\sqrt{8\pi k_\omega \sqrt{M''}}} \sum_{\kappa=1}^M b_\kappa e^{-ik_\omega \exp(i\sigma_{\kappa'}) \cdot x_{i,\kappa}}, \quad \kappa' = 1, \dots, M'', \\ \mathcal{M}\left((b_\kappa), (c_\kappa), (a_l)\right)_{2,\kappa'} &:= \frac{\sqrt{\gamma}}{\sqrt{M}} \sum_{\kappa=1}^M \log \sin^2(\pi[\kappa' - \kappa]/M) b_\kappa, \quad \kappa' = 1, \dots, M, \\ \mathcal{M}\left((b_\kappa), (c_\kappa), (a_l)\right)_{3,\kappa',l} &:= \frac{\sqrt{\gamma}}{\sqrt{M}} \sum_{\kappa=1}^M \log \sin^2(\pi[\kappa' - \kappa]/M) [c_\kappa]_l, \quad \kappa' = 1, \dots, M, \quad l = 1, 2, \\ \mathcal{M}\left((b_\kappa), (c_\kappa), (a_l)\right)_{4,\kappa',l} &:= \frac{1}{\sqrt{M'}} \sum_{\kappa=1}^M [t_{x_{\mathbf{r},\kappa'}} [G^{\text{el}}(x_{e,\kappa}, x_{\mathbf{r},\kappa'}) c_\kappa]]_l \\ &\quad + \frac{1}{\sqrt{M'}} \sum_{\kappa=1}^M b_\kappa G(x_{\mathbf{r},\kappa'}, x_{i,\kappa}) [\nu(x_{\mathbf{r},\kappa'})]_l \\ &\quad + \frac{p^{\text{inc}}(x_{\mathbf{r},\kappa'}) [\nu(x_{\mathbf{r},\kappa'})]_l}{\sqrt{M'}}, \quad \kappa' = 1, \dots, M', \quad l = 1, 2, \\ \mathcal{M}\left((b_\kappa), (c_\kappa), (a_l)\right)_{5,\kappa'} &:= \frac{1}{\sqrt{M'}} \sum_{\kappa=1}^M \nu(x_{\mathbf{r},\kappa'}) \cdot G^{\text{el}}(x_{e,\kappa}, x_{\mathbf{r},\kappa'}) c_\kappa \\ &\quad - \frac{1}{\sqrt{M'} \varrho_f \omega^2} \sum_{\kappa=1}^M b_\kappa \partial_{\nu(x_{\mathbf{r},\kappa'})} G(x_{\mathbf{r},\kappa'}, x_{i,\kappa}) \\ &\quad - \frac{\partial_\nu p^{\text{inc}}(x_{\mathbf{r},\kappa'})}{\sqrt{M'} \varrho_f \omega^2}, \quad \kappa' = 1, \dots, M'. \end{aligned} \quad (6.7)$$

Here we define the expression  $\{\log \sin^2(\pi 0/M)\}$  as 0. This leads to the following formulas for the derivatives. For the first components, we get

$$\begin{aligned} \frac{\partial}{\partial [\Re b_\kappa]} \mathcal{M}\left((b_\kappa), (c_\kappa), (a_l)\right)_{1,\kappa'} &= \frac{e^{i\pi/4}}{\sqrt{8\pi k_\omega \sqrt{M''}}} \begin{pmatrix} \cos(-k_\omega \exp(i\sigma_{\kappa'}) \cdot x_{i,\kappa}) \\ \sin(-k_\omega \exp(i\sigma_{\kappa'}) \cdot x_{i,\kappa}) \end{pmatrix}^\top, \\ \frac{\partial}{\partial [\Im b_\kappa]} \mathcal{M}\left((b_\kappa), (c_\kappa), (a_l)\right)_{1,\kappa'} &= \frac{e^{i\pi/4}}{\sqrt{8\pi k_\omega \sqrt{M''}}} \begin{pmatrix} -\sin(-k_\omega \exp(i\sigma_{\kappa'}) \cdot x_{i,\kappa}) \\ \cos(-k_\omega \exp(i\sigma_{\kappa'}) \cdot x_{i,\kappa}) \end{pmatrix}^\top. \end{aligned}$$



For the second components, we obtain

$$\begin{aligned}\frac{\partial}{\partial[\Re b_\kappa]} \mathcal{M}\left((b_\kappa), (c_\kappa), (a_l)\right)_{2,\kappa'} &= \frac{\sqrt{\gamma}}{\sqrt{M}} \begin{pmatrix} \log \sin^2(\pi[\kappa' - \kappa]/M) \\ 0 \end{pmatrix}^\top, \\ \frac{\partial}{\partial[\Im b_\kappa]} \mathcal{M}\left((b_\kappa), (c_\kappa), (a_l)\right)_{2,\kappa'} &= \frac{\sqrt{\gamma}}{\sqrt{M}} \begin{pmatrix} 0 \\ \log \sin^2(\pi[\kappa' - \kappa]/M) \end{pmatrix}^\top.\end{aligned}$$

For the third components, we have

$$\begin{aligned}\frac{\partial}{\partial[\Re [c_\kappa]_l]} \mathcal{M}\left((b_\kappa), (c_\kappa), (a_l)\right)_{3,\kappa',l'} &= \frac{\sqrt{\gamma}}{\sqrt{M}} \begin{pmatrix} \log \sin^2(\pi[\kappa' - \kappa]/M) \delta_{l,l'} \\ 0 \end{pmatrix}^\top, \\ \frac{\partial}{\partial[\Im [c_\kappa]_l]} \mathcal{M}\left((b_\kappa), (c_\kappa), (a_l)\right)_{3,\kappa',l'} &= \frac{\sqrt{\gamma}}{\sqrt{M}} \begin{pmatrix} 0 \\ \log \sin^2(\pi[\kappa' - \kappa]/M) \delta_{l,l'} \end{pmatrix}^\top.\end{aligned}$$

The derivatives of the fourth components take the form

$$\begin{aligned}\frac{\partial}{\partial[\Re b_\kappa]} \mathcal{M}\left((b_\kappa), (c_\kappa), (a_l)\right)_{4,\kappa',l} &= +\frac{1}{\sqrt{M'}} \begin{pmatrix} \Re G(x_{\mathbf{r},\kappa'}, x_{i,\kappa})[\nu(x_{\mathbf{r},\kappa'})]_l \\ \Im G(x_{\mathbf{r},\kappa'}, x_{i,\kappa})[\nu(x_{\mathbf{r},\kappa'})]_l \end{pmatrix}^\top, \\ \frac{\partial}{\partial[\Im b_\kappa]} \mathcal{M}\left((b_\kappa), (c_\kappa), (a_l)\right)_{4,\kappa',l} &= +\frac{1}{\sqrt{M'}} \begin{pmatrix} -\Im G(x_{\mathbf{r},\kappa'}, x_{i,\kappa})[\nu(x_{\mathbf{r},\kappa'})]_l \\ \Re G(x_{\mathbf{r},\kappa'}, x_{i,\kappa})[\nu(x_{\mathbf{r},\kappa'})]_l \end{pmatrix}^\top, \\ \frac{\partial}{\partial[\Re [c_\kappa]_l]} \mathcal{M}\left((b_\kappa), (c_\kappa), (a_l)\right)_{4,\kappa',l'} &= \\ & \frac{1}{\sqrt{M'}} \begin{pmatrix} [t_{x_{\mathbf{r},\kappa'}}([\Re G^{el}(x_{e,\kappa}, x_{\mathbf{r},\kappa'})]_{m,l})_m]_{l'} \\ [t_{x_{\mathbf{r},\kappa'}}([\Im G^{el}(x_{e,\kappa}, x_{\mathbf{r},\kappa'})]_{m,l})_m]_{l'} \end{pmatrix}^\top, \\ \frac{\partial}{\partial[\Im [c_\kappa]_l]} \mathcal{M}\left((b_\kappa), (c_\kappa), (a_l)\right)_{4,\kappa',l'} &= \\ & \frac{1}{\sqrt{M'}} \begin{pmatrix} -[t_{x_{\mathbf{r},\kappa'}}([\Im G^{el}(x_{e,\kappa}, x_{\mathbf{r},\kappa'})]_{m,l})_m]_{l'} \\ [t_{x_{\mathbf{r},\kappa'}}([\Re G^{el}(x_{e,\kappa}, x_{\mathbf{r},\kappa'})]_{m,l})_m]_{l'} \end{pmatrix}^\top, \\ \frac{\partial}{\partial a_l} \mathcal{M}\left((b_\kappa), (c_\kappa), (a_l)\right)_{4,\kappa',l} &= \\ & \frac{1}{\sqrt{M'}} \sum_{\kappa=1}^M \text{grad}_{x_{\mathbf{r},\kappa'}} [t_{x_{\mathbf{r},\kappa'}} [G^{el}(x_{e,\kappa}, x_{\mathbf{r},\kappa'}) c_\kappa]_l] \frac{\partial}{\partial a_l} [x_{\mathbf{r},\kappa'}] \\ & + \frac{1}{\sqrt{M'}} \sum_{\kappa=1}^M b_\kappa \text{grad}_{x_{\mathbf{r},\kappa'}} [G(x_{\mathbf{r},\kappa'}, x_{i,\kappa})] \frac{\partial}{\partial a_l} [x_{\mathbf{r},\kappa'}] [\nu(x_{\mathbf{r},\kappa'})]_l \\ & + \frac{1}{\sqrt{M'}} \sum_{\kappa=1}^M b_\kappa G(x_{\mathbf{r},\kappa'}, x_{i,\kappa}) \frac{\partial}{\partial a_l} [\nu(x_{\mathbf{r},\kappa'})]_l \\ & + \frac{1}{\sqrt{M'}} \text{grad}_{x_{\mathbf{r},\kappa'}} [p^{inc}(x_{\mathbf{r},\kappa'})] \frac{\partial}{\partial a_l} [x_{\mathbf{r},\kappa'}] [\nu(x_{\mathbf{r},\kappa'})]_l \\ & + \frac{1}{\sqrt{\#K_{M'}}} p^{inc}(x_{\mathbf{r},\kappa'}) \frac{\partial}{\partial a_l} [\nu(x_{\mathbf{r},\kappa'})]_l.\end{aligned}$$

Finally, for the fifth components, we obtain

$$\begin{aligned}
\frac{\partial}{\partial[\Re b_\kappa]} \mathcal{M}\left((b_\kappa), (c_\kappa), (a_l)\right)_{5,\kappa'} &= -\frac{1}{\sqrt{M'} \varrho_f \omega^2} \begin{pmatrix} \partial_{\nu(x_{\mathbf{r},\kappa'})} \Re G(x_{\mathbf{r},\kappa'}, x_{i,\kappa}) \\ \partial_{\nu(x_{\mathbf{r},\kappa'})} \Im G(x_{\mathbf{r},\kappa'}, x_{i,\kappa}) \end{pmatrix}^\top, \\
\frac{\partial}{\partial[\Im b_\kappa]} \mathcal{M}\left((b_\kappa), (c_\kappa), (a_l)\right)_{5,\kappa'} &= -\frac{1}{\sqrt{M'} \varrho_f \omega^2} \begin{pmatrix} -\partial_{\nu(x_{\mathbf{r},\kappa'})} \Im G(x_{\mathbf{r},\kappa'}, x_{i,\kappa}) \\ \partial_{\nu(x_{\mathbf{r},\kappa'})} \Re G(x_{\mathbf{r},\kappa'}, x_{i,\kappa}) \end{pmatrix}^\top, \\
\frac{\partial}{\partial[\Re [c_\kappa]_l]} \mathcal{M}\left((b_\kappa), (c_\kappa), (a_l)\right)_{5,\kappa'} &= \\
&\frac{1}{\sqrt{M'}} \begin{pmatrix} \nu(x_{\mathbf{r},\kappa'}) \cdot (\Re [G^{el}(x_{\mathbf{r},\kappa'}, x_{i,\kappa})]_{m,l})_m \\ \nu(x_{\mathbf{r},\kappa'}) \cdot (\Im [G^{el}(x_{\mathbf{r},\kappa'}, x_{i,\kappa})]_{m,l})_m \end{pmatrix}^\top, \\
\frac{\partial}{\partial[\Im [c_\kappa]_l]} \mathcal{M}\left((b_\kappa), (c_\kappa), (a_l)\right)_{5,\kappa'} &= \\
&\frac{1}{\sqrt{M'}} \begin{pmatrix} -\nu(x_{\mathbf{r},\kappa'}) \cdot (\Im [G^{el}(x_{\mathbf{r},\kappa'}, x_{i,\kappa})]_{m,l})_m \\ \nu(x_{\mathbf{r},\kappa'}) \cdot (\Re [G^{el}(x_{\mathbf{r},\kappa'}, x_{i,\kappa})]_{m,l})_m \end{pmatrix}^\top, \\
\frac{\partial}{\partial a_l} \mathcal{M}\left((b_\kappa), (c_\kappa), (a_l)\right)_{5,\kappa'} &= \frac{1}{\sqrt{M'}} \sum_{\kappa=1}^M {}^\top [G^{el}(x_{e,\kappa}, x_{\mathbf{r},\kappa'}) c_\kappa] \frac{\partial}{\partial a_l} [\nu(x_{\mathbf{r},\kappa'})] + \\
&\frac{1}{\sqrt{M'}} \sum_{\kappa=1}^M \nu(x_{\mathbf{r},\kappa'}) \cdot \text{grad}_{x_{\mathbf{r},\kappa'}} [G^{el}(x_{e,\kappa}, x_{\mathbf{r},\kappa'}) c_\kappa] \frac{\partial}{\partial a_l} [x_{\mathbf{r},\kappa'}] \\
&- \frac{1}{\sqrt{M'} \varrho_f \omega^2} \sum_{\kappa=1}^M {}^\top [b_\kappa \text{grad}_{x_{\mathbf{r},\kappa'}} G(x_{\mathbf{r},\kappa'}, x_{i,\kappa})] \frac{\partial}{\partial a_l} [\nu(x_{\mathbf{r},\kappa'})] \\
&- \frac{1}{\sqrt{M'} \varrho_f \omega^2} \sum_{\kappa=1}^M b_\kappa \nu(x_{\mathbf{r},\kappa'}) \cdot \text{grad}_{x_{\mathbf{r},\kappa'}} [\text{grad}_{x_{\mathbf{r},\kappa'}} G(x_{\mathbf{r},\kappa'}, x_{i,\kappa})] \frac{\partial}{\partial a_l} [x_{\mathbf{r},\kappa'}] \\
&- \frac{1}{\sqrt{M'} \varrho_f \omega^2} {}^\top [\text{grad}_{x_{\mathbf{r},\kappa'}} p^{inc}(x_{\mathbf{r},\kappa'})] \frac{\partial}{\partial a_l} [\nu(x_{\mathbf{r},\kappa'})] \\
&- \frac{1}{\sqrt{M'} \varrho_f \omega^2} \nu(x_{\mathbf{r},\kappa'}) \cdot \text{grad}_{x_{\mathbf{r},\kappa'}} [\text{grad}_{x_{\mathbf{r},\kappa'}} p^{inc}(x_{\mathbf{r},\kappa'})] \frac{\partial}{\partial a_l} [x_{\mathbf{r},\kappa'}].
\end{aligned}$$

## References

- [1] M. Abramowitz and A. Stegun, *Handbook of mathematical functions*, National Bureau of Standards, Applied Mathematics Series **55**, Washington, 1964.
- [2] A.H. Barnett and T. Betcke, Stability and convergence of the method of fundamental solutions for Helmholtz problems on analytic domains, *Journal Comp. Physics*, **227**, (2008), pp. 7003–7026.
- [3] D. Colton and R. Kress, *Inverse acoustic and electromagnetic scattering theory*, Applied Mathematical Sciences **93**, Springer-Verlag, Berlin, Heidelberg, New York, 2nd ed., 1998.

- [4] J. Elschner, G.C. Hsiao, and A. Rathsfeld, An inverse problem for fluid-solid interaction, *Inverse Problems and Imaging* **2**, (2008), pp. 83-120.
- [5] J. Elschner, G.C. Hsiao, and A. Rathsfeld, An optimization method in inverse acoustic scattering by an elastic obstacle, *SIAM Journal Appl.Math.* **70**, (2009), pp. 168–187.
- [6] M.A. Golberg and C.S. Chen, *Discrete projection methods for integral equations*, Computational Mechanics Publications, Southampton, Boston, 1997.
- [7] Ch. Hafner, *The generalized multipole technique for computational electromagnetics*, Artech House Books, Boston 1990.
- [8] T. Hargé, Valeurs propres d'un corps élastique, *C.R. Acad. Sci. Paris*, **311**, Série I (1990), 857–859.
- [9] J. Hoffmann, Ch. Hafner, P. Leidenberger, J. Hesselbarth, and S. Burger, Comparison of electromagnetic field solvers for the 3D analysis of plasmonic nanoantennas, in *Modeling Aspects in Optical Metrology II*, eds.: H. Bosse, B. Bodermann, and R.M. Silver, Proceedings of SPIE **7390**, 2009, pp. 73900J-1–73900J-11.
- [10] G.C. Hsiao and W.L. Wendland, *Boundary integral equations*, Applied Mathematical Sciences **164**, Springer-Verlag, Berlin, Heidelberg, 2008.
- [11] A. Kirsch and N. Grinberg, *The factorization method for inverse problems*, Oxford Lectures in Mathematics and its Applications **38**, Oxford University Press, Oxford, 2009.
- [12] A. Kirsch and R. Kress, An optimization method in inverse acoustic scattering, In: *Boundary elements IX*, Vol. 3, (eds.: C.A. Brebbia et al), Springer-Verlag, Berlin etc., 1987, pp. 3–18.
- [13] M. Lourakis, <http://www.ics.forth.gr/~lourakis/levmar>
- [14] O. Ivanyshyn, R. Kress, and P. Serranho, Huygens' principle and iterative methods in inverse obstacle scattering, *Advances Comput. Math.*, to appear.
- [15] P. Monk and V. Selgas, An inverse fluid-solid interaction problem, *Inverse Problems and Imaging* **3**, (2009), pp. 173–198.
- [16] D. Natroshvili, G. Sadunishvili, and I. Sigua, Some remarks concerning Jones eigenfrequencies and Jones modes, *Georgian Mathematical Journal*, **12** (2005), 337–348.
- [17] J. Nocedal and S.J. Wright, *Numerical optimization*, Springer-Verlag, New-York Berlin Heidelberg, Springer Series in Operation Research, 2000.
- [18] O. Schenk, K. Gärtner, and W. Fichtner, Efficient sparse LU factorization with left-right looking strategy on shared memory multiprocessors, *BIT*, **40** (2000), 158–176.
- [19] J. Schöberl, NETGEN: An advancing front 2D/3D-mesh generator based on abstract rules, *Comput. Vis. Sci.*, **1** (1997), 41-52.

- [20] A. Zinn, The numerical solution of an inverse scattering problem for time-harmonic acoustic waves, In: *Inverse Problems and Imaging*, (ed.: F. Roach), Pitman Research Notes in Mathematical Sciences **245**, Longman, London, 1991, pp. 242–263.